In presenting the dissertation as a partial fulfillment of the requirements for an advanced degree from the Georgia Institute of Technology, I agree that the Library of the Institute shall make it available for inspection and circulation in accordance with its regulations governing materials of this type. I agree that permission to copy from, or to publish from, this dissertation may be granted by the professor under whose direction it was written, or, in his absence, by the Dean of the Graduate Division when such copying or publication is solely for scholarly purposes and does not involve potential financial gain. It is understood that any copying from, or publication of, this dissertation which involves potential financial gain will not be allowed without written permission.

7/25/68

ADSORPTION OF CARBON MONOXIDE ON RUTHENIUM

A THESIS

Presented to

The Faculty of the Division of Graduate

Studies and Research

by

Saghana Baran Chakrabortty

In Partial Fulfillment

of the Requirements for the Degree

Master of Science in Metallurgy

Georgia Institute of Technology

June 1971

ADSORPTION OF CARBON MONOXIDE ON RUTHENIUM

Approved:

Chairman

Date approved by Chairman: 5/31/71

ACKNOWLEDGMENTS

The author wishes to express his gratitude to his thesis advisor, Dr. Helen E. Grenga, for her inspiring guidance, sustained encouragement and helpful suggestions.

He is also grateful to Dr. Robert F. Hochman and Dr. Bruce G. LeFevre for having taken time to review this work.

The help rendered by the graduate students and faculty members in metallurgy is also deeply appreciated. The author is thankful to Dr. John Burson for his help in computer programming.

The financial support of this research provided by National Science Foundation is gratefully acknowledged.

TABLE OF CONTENTS

TABLE OF CONTENTS (Continued)

LIST OF TABLES

LIST OF FIGURES

LIST OF FIGURES (Continued)

SUMMARY

Chemisorption is the initial stage of any heterogeneous catalytic reaction. Carbon monoxide is chemisorbed by transition metals, in general, but only certain metals, for example, iron, cobalt, nickel and ruthenium can be successfully used as catalysts for the decomposition of carbon monoxide and for the production of hydrocarbons from carbon monoxide and hydrogen. Furthermore, the activity of these metals depends on the crystal orientation. It is therefore expected that the catalytic activity for a given metal and orientation depends on the types of chemisorption states formed on the surface. The purpose of this research was to investigate the crystallographic specificity of chemisorption states of carbon monoxide on ruthenium.

Field-ion and emission microscopy techniques were used to study the adsorption and desorption of carbon monoxide on the $(10\bar{1}1)$, $(10\bar{1}0)$, $(11\bar{2}2)$ and $(20\bar{2}1)$ regions of ruthenium. Field-ion microscopy was used to clean and characterize the ruthenium prior to carbon monoxide adsorption, while field-emission microscopy was used to measure the work function of a single crystal region before and after adsorption. In the desorption experiments, the work function of a single crystal region was measured after each stage of desorption at a given field. From these studies the chemisorption states of carbon monoxide on ruthenium were identified.

The work function of ruthenium increased upon adsorption of carbon

monoxide. An electropositive α state of carbon monoxide was found on the $(10\bar{1}1)$ and $(10\bar{1}0)$ low index regions, but not on the $(11\bar{2}2)$ and $(20\bar{2}1)$ regions. The electronegative β state was found on all the regions investigated. It was also observed that the extent of interaction and/or the amount of α and β states varied with crystal region. Strong evidence of surface reconstruction during field desorption was present for all the regions of ruthenium investigated. The desorption field for the β state on ruthenium was found to be lower than that reported for the β state on tungsten, indicating that carbon monoxide is bound less strongly on ruthenium than on tungsten. However, the work function change upon adsorption of carbon monoxide was greater for ruthenium than for tungsten.

CHAPTER I

INTRODUCTION AND LITERATURE SURVEY

1.1. Introduction

The reaction of carbon monoxide with metals is an important and complex problem at many levels of academic and applied interests. Recently, this problem has been attacked on a fundamental level to understand the mechanism of the reaction. Depending upon the gas-metal system involved this reaction can be either beneficial (Fischer-Tropsch synthesis) or destructive (metal dusting).

Metals like iron, cobalt, nickel and ruthenium are widely used as catalysts in various reactions where carbon monoxide is one of the reactants. A metal acting as a catalyst adsorbs at least one of the reactants. The chemical properties of this reactant are changed during the chemisorption process and this interaction helps the occurrence of the proper reaction with the other reactant(s) to give rise to the desired product. Thus for the development of efficient catalysts, the study of the nature of chemisorption and the properties of the chemisorbed species is of primary importance.

The reaction occurring between carbon monoxide and metal varies, depending primarily upon the chemical nature of the metal and the temperature. At lower temperatures chemical bonds between metal atoms and the CO molecules are formed and carbonyls for some metals are known to result, notably iron, cobalt and nickel. At higher temperatures catalytic decomposition of carbon

monoxide occurs on these metals and free graphite or carbide may form. For example, the reaction of carbon monoxide with nickel at 550°C produces primarily graphite on the nickel surface while the reaction with iron produces carbides. These reactions on single crystal films have recently been studied by Grenga (1) for nickel and Ratliff (2) for iron.

In 1925 Taylor proposed the existence of certain active sites on the surface of the catalyst. Since then it has been shown that only a small fraction of the metal surface is usually active in the catalytic reaction. A number of workers related the activity to the presence of dislocations. Gwathmey, et al (3-5) demonstrated the influence of the crystallographic orientation on the catalytic activity. For the reaction of carbon monoxide on nickel, graphite deposits are formed primarily on regions near the {111} poles. Grenga (1), using transmission electron microscopy on single crystal nickel thin film showed that the active sites for this reaction on nickel were surface steps rather than dislocations.

Since chemisorption is the initial stage in the catalytic reaction, it is expected that the difference in activity of various catalytic orientations and at different sites on a given orientation are related to chemisorption behavior.

The purpose of this investigation was to study the chemisorption of carbon monoxide on ruthenium to reveal the crystallographic specificity of chemisorption states in such a system. Ruthenium was chosen for two reasons. First, it is an important catalyst which is used for production of high molecular weight hydrocarbons, and second, ruthenium is the most suitable of the Fischer-Tropsch catalysts for the field-ionization and field-emission techniques used in this

investigation. While these techniques are capable of revealing adsorption states on a given crystallographic region, only refractory or near refractory metals may be used.

1.2. Field-Emission Microscopy (6)

Field emission is the emission of electrons from the surface of a condensed phase into another phase usually vacuum, under the action of high electrostatic fields (0.3 to 0.6 volt/angstrom). In the case of metal-vacuum interfaces, this phenomenon of electron emission consists of tunneling of electrons through the deformed potential barrier at the surface. The surface potential is important in determining the emission current, and for this reason field emission can be applied to study a variety of surface phenomena.

1.2.1. Electronic Properties of Surfaces

The solid state analogue of the ionization potential in atoms or molecules is called the work function, ϕ, and corresponds to the energy difference between the fermi energy, μ and a field free vacuum near the surface. If a metal surface is planar on atomic scale, the electron cloud in the metal will not terminate abruptly since it would correspond to an infinite gradient of wave function and hence infinite kinetic energy. Instead there will be a gradual decay (Figure 1). This spill-over causes a double layer or condensor on the surface with negative side on outer surface. The surface potential thus created increases the work function. In the case of loosely packed planes the surface potential will be positive because a second kind of spill-over, where electrons flow into the concave portions in the surface, exposes corners denuded of electrons. Thus the work

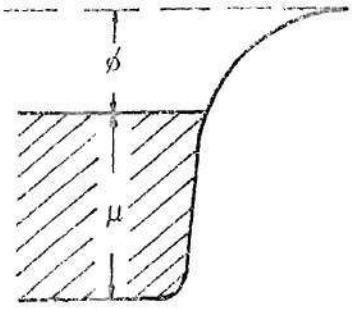

Figure 1. Potential-Energy Diagram for Electrons at a Metal Surface (Image Potential Included): μ is Fermi Energy; ϕ is Work Function.

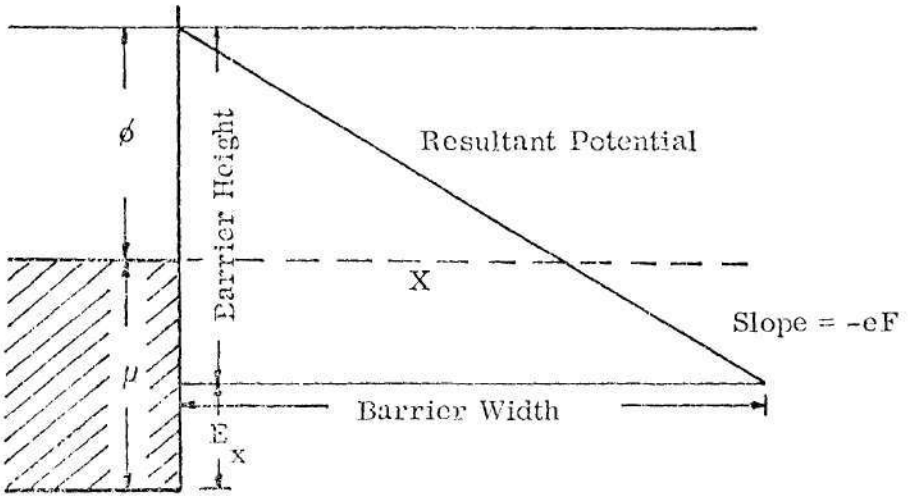

Figure 2. Potential Energy Diagram for Electrons at a Metal Surface (Image Potential not Included) in the Presence of an Applied Field. The Barrier Height and Barrier Width for an Electron with Energy E_x are shown.

function will be less for the loosely packed planes compared to that for the closely packed planes.

Adsorption also causes surface double layers. An adsorbed atom or molecule has a dipole moment, p_i, associated with it. If these dipoles are completely contained in the adsorbed layer, this causes a surface potential, χ, according to the relation

$$\chi = \sum_i 4\pi N_i p_i \qquad (1)$$

where N_i is the number of adsorbed particles (ad-particles) each having a dipole moment p_i. A surface potential is positive when the dipoles point outward with their positive ends.

The surface potential changes the work function at that surface according to:

$$\chi = - \frac{\Delta \phi}{e} \qquad (2)$$

where $\Delta\phi$ is the change in work function and e is the electronic charge. Thus a negative dipole moment causes an increase and positive dipole moment a decrease in the work function.

1.2.2. Field-Emission Current

When the applied field is strong enough, the potential barrier at the metal surface is deformed such that unexcited electrons can "leak" through it. When a field, F, is applied to the metal surface electrons with kinetic energy E_x along the emission direction see a barrier of height $\phi + \mu - E_x$ and of thickness

$(\phi + \mu - E_x)/eF$ (Figure 2). If this barrier is thin and low enough, these electrons will tunnel from the metal with finite probability. The maximum energy of the electrons is μ and the maximum barrier height and width will be approximately ϕ and ϕ/eF respectively.

Applying quantum mechanics and considering tunneling of all electrons with the kinetic energy range $0 \leq E_x \leq \mu$, Fowler and Nordheim (7) formed the equation for emission at $0^{o}K$ as:

$$i = a' \frac{(\mu/\phi)^{\frac{1}{2}}}{\mu+\phi} F^2 \exp(-b' \frac{\phi^{3/2}}{F}) \tag{3}$$

Where i is the current density of electron emission and a′ and b′ are constants. Including the image potential the equation (3) changes

to:
$$i = a' \frac{(\mu/\phi)^{\frac{1}{2}}}{\alpha^2(\mu+\phi)} F^2 \exp(-b' \alpha \frac{\phi^{3/2}}{F}) \tag{4}$$

where
$$\alpha = (1 - 3.8 \times 10^{-4} F^{\frac{1}{2}}/\phi)^2$$

Thus equation (4) can be changed to:

$$I = a' \frac{(\mu/\phi)^{\frac{1}{2}}}{\alpha^2(\mu+\phi)} \frac{V^2}{\beta^2} A_e \exp(-b' \beta \frac{\phi^{3/2}}{V}) \tag{5}$$

where A_e is the emitting area relating I and i by $I = A_e \cdot i$ and β is a geometric factor relating V and F by the equation, $V = \beta F$.

Thus a plot of $\log(I/V^2)$ versus $1/V$ gives a curve with the slope given by:

$$m = -b' \phi^{3/2} \cdot f(\alpha). \tag{6}$$

Since $f(\alpha)$ is a slowly varying function of F and is close to unity, the plot approaches a straight line and the slope is given by:

$$m = -b \phi^{3/2} \tag{7}$$

where b is almost independent of ϕ and F.

Using equations (2) and (7) the surface potential due to the adsorbed species can be determined if the ϕ value of the clean surface is known and the slopes for the clean surface (m_{cl}) and for the surface after adsorption (m_{ad}) are measured. Assuming b does not change upon adsorption the change in ϕ, $\Delta\phi_{ad}$, due to adsorption is given by the relation:

$$\phi_{cl} + \Delta\phi_{ad} = (m_{ad}/m_{cl})^{2/3} \cdot \phi_{cl} \tag{8}$$

then the value of $\Delta\phi_{ad}$ can be used to calculate the surface potential.

1.2.3. Pre-exponential in the Fowler-Nordheim Equation

The Fowler-Nordheim (F-N) equation can be written in the form

$$I = AV^2 \exp\left(-B \frac{\phi^{3/2}}{V}\right) \tag{9}$$

where A is the pre-exponential factor and depends upon ϕ, μ, emitting area and

the properties of the adsorbed layer, if present. The pre-exponential factor is fairly independent of the applied field. The factor B depends upon the specimen geometry and is independent of ϕ and V.

Methods have been used where the measurements of current at a constant voltage or the voltage required for a constant emission were done to indicate the changes in ϕ during adsorption or desorption. In such procedures A was assumed to be unchanged upon adsorption, or with various degrees of desorption. Very often, however, large changes in A are observed, and measurements of the ϕ changes from F-N plots are mandatory.

There are several causes for changes in A during adsorption and desorption. The emitting area may change during adsorption and cause an increase in A when the total emission is measured. Menzel and Gomer (8) propose that the electrostatic field polarizes the ad-layer and thus increases the work function and decreases the emission current and the pre-exponential factor. The slope of the F-N plot, however, remains unaffected by the polarization, because the degree of polarization is proportional to the field strength.

According to Van Oostrom (9) the physisorbed layer modifies the image potential such that the resulting barrier for the electrons becomes larger. This reduces the emission intensity and therefore A.

Holscher (10) proposes that the formation of the "corrosive" chemisorption layer decreases the value of A. The "corrosive" chemisorption (see sec. 1.4.4) leads to changes in atom positions in the outermost layer of the metal and thus a dielectric film is formed on the metal surface due to this "demetallization." This

layer not only modifies the potential barrier, but probably also reduces the transmission of electrons even further by confronting them with an additional barrier. Scattering of the conduction electrons occurs due to the disturbances in the periodic potential caused by the "corrosive chemisorption." This increases the resistance of the surface layer and thus reduces the supply of the transmitting electrons, thereby decreasing A.

While adsorption and "corrosive chemisorption" may lead to decrease in A as discussed above, desorption of these species obviously would lead to increases in the value of A.

1.2.4. Field-Emission Microscope (6, 11)

A schematic diagram of a typical field-emission microscope is shown in Figure 3. To avoid any interaction between the emitted electrons and the gas particles present in the chamber, the microscope chamber is evacuated; for this purpose a pressure at 10^{-7} torr range is adequate. To keep the emitter uncontaminated for a long time however, a pressure as low as 10^{-10} to 10^{-11} torr is a necessity.

The specimen is an electropolished wire with almost hemispherical tip. The field at the tip of radius r and potential V is given by:

$$F = V/k \cdot r,$$

where k is a constant due to presence of the conical shank; k is about 5 near the apex and increases with the increase in polar angle. Thus for a tip with a radius of 500 Å, 1 to 2.5 KV potential gives the adequate field.

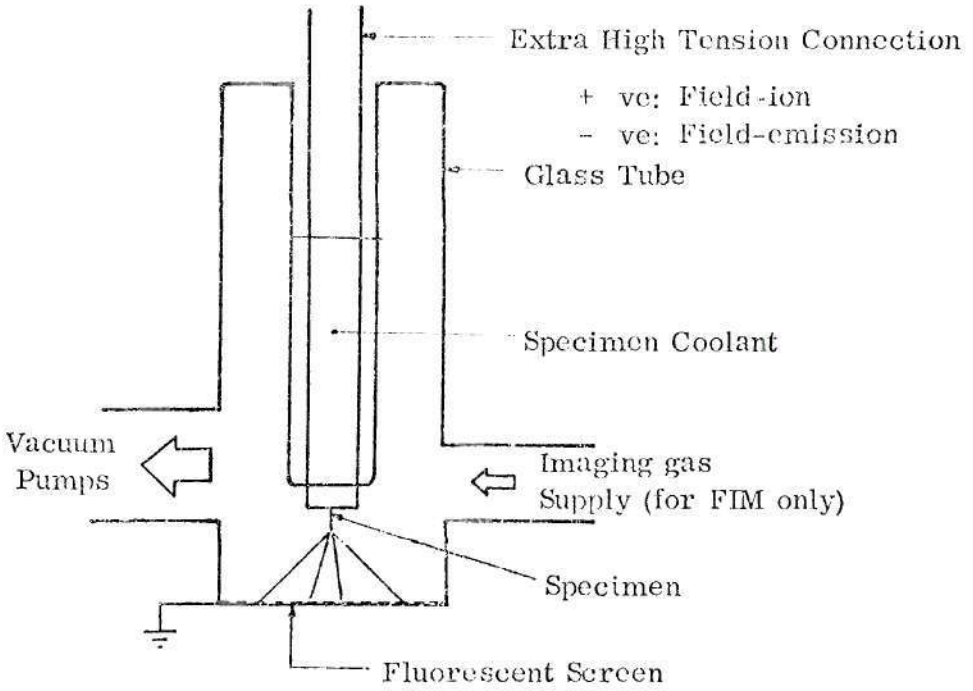

Figure 3. Schematic Diagram of Field-Ion/-Emission Microscope.

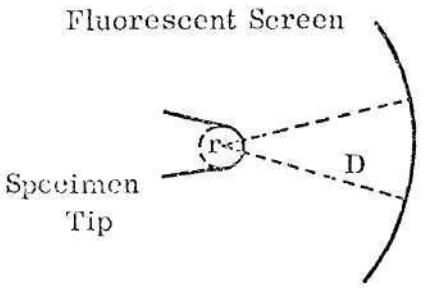

Figure 4. Schematic Diagram of Trajectories of Field Emitted Electrons, Showing Mechanism of Image Formation.

The electrons that have just emerged from the barrier have very little kinetic energy and therefore follow the lines of force, at least initially. Since the emitter is a conductor and hence has an equipotential surface, lines of force are orthogonal to it and diverge radially outward from the tip. If a conducting fluorescent screen as the anode is placed in front of the emitter, the diverging electrons will produce a very much magnified image of the tip on the fluorescent screen (Figure 4). Ideally the magnification will be given by D/r, where r is the tip radius and D is the tip to screen distance. However the emitter shank compresses the lines of force originating at the tip toward the longitudinal axis; so the actual magnification is given approximately by D/1.5r.

The resolution of the field-emission image is not as high as that of a field ion image. The electron emitted out of the metal carry with it some lateral momentum. This added with the quantum mechanical Heisenberg uncertainty principle limit the resolution of the field-emission image to 25 $\mathring{A}$. Thus atomic details cannot be seen on such image.

The spherical surface of the FEM tip exposes flat facets of low surface energy, blending smoothly into curved regions of continuously varying indices. Since the work function depends upon the orientation the pattern shows an emission anisotropy corresponding to the crystal symmetry. The low index planes with high work function image as dark portions on the screen. The field-emission pattern can be indexed by the method given for the field-ion image.

Local variation in the field may occur whenever the local radius of curvature differs from that of the main tip. This also adds to the contrast in the field

emission image.

1.3. Field-ion Microscopy

Field ionization consists of electrons tunneling from atoms under the action of much higher electric fields (2 to 5V/Å) than for field emission. The magnification of the field ion microscope is better than a million times and the resolution is 2-3 Å for conventional helium-ion microscopy. Therefore field-ion microscopy can be applied to characterize the surface structure of solids on an atomic level. Furthermore, due to the process of field evaporation and field desorption, adsorbed species as well as metal atoms can be removed from the surface to produce a clean atomically characterized surface.

1.3.1. Field Ionization

The mechanism of field ionization of a free atom or molecule is analogous to that of field emission from a metal. An electron tunnels through a potential barrier which is distorted by a high electric field, the barrier width at a given field strength now being determined by the ionization potential, I, of the atom or molecule. Since the value of the ionization potentials of the most simple gases are much higher than the work functions of metals, the field strength required for field ionization is much higher (roughly by a factor of ten) than that required for field emission.

The electric field increases the supply of gas atoms to a region near the surface where the ionization occurs. Gas atoms passing near the surface are polarized by the electric field and are then attracted toward the region of strongest

field at the tip surface. After striking the tip and bouncing away they are attracted back to it. These atoms may bounce several times at the cryogenically cooled tip until they lose enough energy so that ionization can occur.

1.3.2. Field-ion Microscope

The field-ion microscope is similar to the field-emission microscope shown in Figure 3. The important differences for field ionization are that the specimen is kept at a positive potential, the applied voltage will be approximately ten times higher than for field emission and the imaging gas at a pressure usually in micron range is used. The specimen, the imaging gas and the microscope wall are cooled to a low temperature, usually 77^{o}K or 21^{o}K. Helium is usually used as imaging gas. Helium ionizes at about 4.5 V/$\mathring{A}$ and therefore can only be used to image those metals that require a field greater than 4.5 V/$\mathring{A}$ for evaporation (see section 1.3.3).

Under typical operating conditions the sharply pointed specimen has a radius of curvature between 100 and 1000 $\mathring{A}$. A positive potential of 3 to 30 kilovolts is applied to the specimen. Helium is ionized at the specimen surface and is attracted towards a collector, which in this case is the fluorescent screen kept at ground potential. Unlike the field-emitted electrons the field-emitted ions have negligible tangential velocity and also are less affected by the uncertainty principles. Therefore the resoltuion is much better in field-ion microscopy (2 to 3 $\mathring{A}$) and an image of atoms on the specimen surface is formed on the screen.

1.3.3. Field Evaporation

Removal of contamination from the surface of the specimen and smoothing

of the tip is achieved by the field evaporation process. If the applied positive potential is increased to a sufficiently high value, it is possible to remove metal ions from the surface; the critical field at which this occurs is known as the evaporation field, F_E. Once this field is exceeded the evaporation occurs very fast. In order to obtain a stable image the ionization field for the imaging gas should be considerably lower than the evaporation field for the specimen.

Field evaporation is a quite complicated process. The basic theory is given by Müller (12, 13). In the absence of an electric field the desorption energy, Q_D, required by an atom to leave the surface as a positive ion will be given by:

$$Q_D = \Lambda + I_n - n \cdot \phi \tag{10}$$

where Λ is the sublimation energy of the evaporating atom, I_n is the nth ionization energy of the metal or the complex evaporated and ϕ is the local work function or the energy carried back to the bulk by the n electrons from the metal atom or complex evaporated. When a field is applied the actual potential barrier, Q, becomes:

$$Q = Q_D - n^3 \cdot e^3 \cdot F \tag{11}$$

and the time, τ, within which this barrier is overcome by the thermal activation is given by:

$$\tau = \tau_0 \exp(Q/kT)$$

where τ_0 is the vibrational time of the atom to be evaporated.

An addition of a polarization term to Q_D, which can be written as $(1/2)\cdot(\alpha_a-\alpha_i)F^2$ where the α's represent the polarizabilities of the atom at its surface site and as a free atom respectively, gives:

$$F_E = n^{-3}\cdot e^{-3}\cdot[\Lambda + I_n - n\phi + 1/2\ (\alpha_a-\alpha_i)F_E^{\ 2} - kT\ \ln(\tau/\tau_0)] \qquad (12)$$

1.3.4. Field Desorption

The field desorption phenomenon (14) is very similar to that of field evaporation. In this case, however, an adsorbed atom or molecule is ionized and removed from the specimen surface. The theory of field desorption is presented by Gomer (6) and by Swanson and Gomer (15). An electron may tunnel from the metal-adsorbate bond into the metal when the bonding level is raised to the Fermi level by vibrational excitation in the presence of a high field, so that the adsorbed particle spends a certain time (τ) beyond a critical distance X_c.

Field desorption can be represented in terms of potential energy diagrams of the metal-adsorbate system as shown in Figure 5 (6), which is drawn for covalent chemisorption of an adsorbate, A, on metal, M. The lower curve of Figure 5a represents the potential energy of the unionized state of metal and adsorbate, and the upper curve is the potential energy of the ionized state with the distance from the surface given as X. There is a set of such ionized states depending upon the electronic energy level in the metal into which the electron from the adsorbate goes. When the electron goes to the lowest available level, i.e., the Fermi level, the energy separation between the ionized and the unionized states at large X will be $I - \phi$.

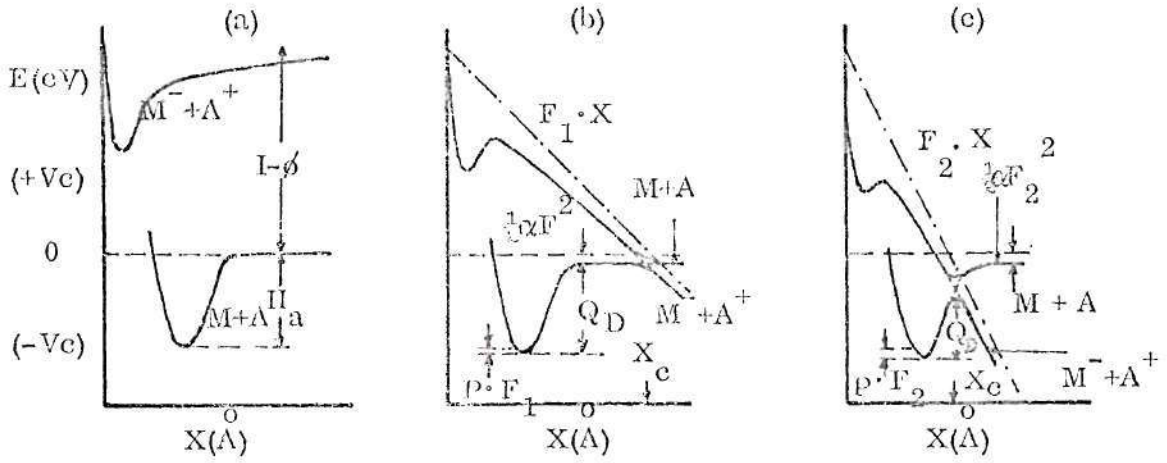

Figure 5. Potential Energy Diagram Illustrating Field Desorption of an Adsorbate A, on a Metal M: I is the Ionization Potential of A; ϕ is the Work Function of M; H_a is the Heat of Adsorption of A on M; Q_D is the Activation Energy for Desorption of A from Metal; P is the Dipole Moment of A, and α is the Polarizability of A; (a) Without Field, (b) with Field F_1 of Moderate Strength and (c) with High Field F_2.

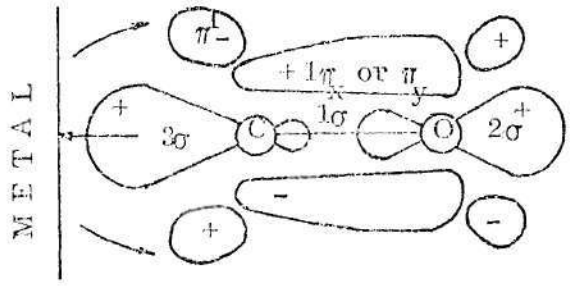

Figure 6. The Molecular Orbitals (Schematic) of Gaseous Carbon Monoxide. Arrows Indicate Possible Interactions of CO with Metal that May Occur in Chemisorption.

When a moderate field F_1 is applied (Figure 5b) the $M^- + A^+$ curve is greatly deformed and the curves for M + A and $M^- + A^+$ intersect at X_c. This gives rise to two new states represented by the solid lines. Supply of an activation energy of Q_D which is almost equal to the heat of adsorption of an adsorbed atom, H_a, leads to desorption of neutral A in the first instance. However as A moves away from the metal surface it may get ionized at X_c whereupon the system follows the lower curve (adiabatic transition). If the time spent in the transition region is short compared to the characteristic time, τ, the chance of tunneling is small and the system does not change to $M^- + A^+$ curve (non-adiabatic transition).

When the resonance separation between the two states is small, τ is large and the transition probability is amall. In Figure 5b the resonance separation decreases with increasing X_c, and the transition probability is small.

When a much higher field is applied (Figure 5c) X_c lies within the attractive part of the ground state curve. Q_D in this case is much less than H_a. This barrier can be overcome by vibrational excitation and ionic desorption may occur. Since the resonance separation between the states is large due to small X_c, it can be assumed that a particle which has the required energy to pass over the barrier will go through the transition. Q_D can be approximated as: $Q_D = V(X_c) + H_a$ where $V(X_c)$ is the potential energy of the field free covalent state at X_c. $V(X_c)$ is negative and V(X) approaches zero as X approaches infinity. Thus by increasing the field, X_c is decreased as is Q_D.

The higher the bond strength or larger the value of H_a, the smaller will be the distance X_c required for successful transition to the ionized states and

subsequent field desorption. Therefore, the desorption of weakly bonded species will require a positive field of less strength than that required for strongly chemisorbed species. Thus from the desorption potential of an adsorbed species the nature of the interaction can be known. Field desorption can therefore be used to identify the chemisorption states.

1.4. Adsorption of Carbon Monoxide to the Transition Metals

The literature on carbon monoxide adsorption on transition metals is voluminous and only the most recent literature is discussed here.

1.4.1. Bonds Between Carbon Monoxide and Transition Metals

For natural reasons the bonds formed in the adsorption of CO on transition metals is believed to be analogous to those in carbonyls. Carbon monoxide in the gaseous phase exhibits a dipole moment of 0.1 D (16); the negative pole is thought to be positioned at the carbon atom end of the molecule. The molecular orbital (MO) theory has been used to explain the bonding within the CO molecule (16) and that between CO and transition metals (17). The MO's for CO are shown schematically in Figure 6; the arrows indicate the possible interactions between CO and transition metals (18). The bonding in an isolated CO molecule is regarded as a result of an sp_z-hybrid orbital of C atom combining with the p_z-orbital of the O atom to produce a σ-bond (1σ) and the p_x- and p_y- orbitals of the C and O atoms combining to produce two π-bonds ($1\pi_x$ and $1\pi_y$). This leaves a lone pair of electrons on the oxygen 2s orbital (2σ) and a lone pair in a C sp_z-hybrid orbital (3σ). In the π-orbitals the electron density is higher near the oxygen side. It is believed

that due to the 3σ protruding away from the center more than the 2σ the negative charge lies on the carbon side. The asymmetric nature of the $1\pi_y$- and $1\pi_x$-MO's, however, nearly offsets the effect of the O-orbital, and so only a small dipole moment is observed.

According to Blyholder (17), the lone pair of C sp_z-hybrid orbital donates an electron to the d-orbital of the metal atom. This forms a σ-bond between the carbon atom and the metal atom. Since the formation of this σ-bond puts a formal negative charge on the metal atom, it is believed that back donation from the metal d-orbital to the antibonding π^+ -MO of CO occurs to remove the excess charge and stabilize the metal-carbon bond.

Blyholder also suggests that π-MO's are formed combining a metal d-orbital, carbon p-orbital and an oxygen p-orbital. The three π-orbitals thus formed will be Ψ_1, Ψ_2, and Ψ_3 π-MOs, where $E_1 < E_2 < E_3$. The Ψ_1 π-orbital strengthens both the C-O and M-O bonds. The second orbital, $\Psi_2\pi$, strengthens M-C bond but weakens C-O bond. For carbonyls, the Ψ_2 π-MO will not be completely filled and Ψ_3 π-MO is empty.

In applying the above considerations to chemisorption problems, Blyholder pointed out that a metal atom can be considered as a central atom in a complex with surrounding metal atoms and the chemicorbed CO molecule(s) as ligands. As the surrounding metal atoms and CO molecules increases, the competition for electron to fill Ψ_2 π-orbital increases and so the strength of the M-C bond decreases.

The σ-bond formed between the lone pair of electrons in the carbon and

the d-electrons of the metal has a positive dipole moment associated with it, whereas the π-bonding between metal, carbon and oxygen has a negative dipole moment associated with it (19). As the competition for d-electrons increases with the coverage, the interaction between a CO molecule and the metal atom(s) changes with the coverage and so also the dipole moment of the adsorbed CO.

The Ψ_2 π-MO will be filled up more as the number of empty d-orbitals increases. As a consequence the negative dipole moment of adsorbed CO will be increased. This is experimentally verified for adsorption on Fe, Co and Ni (19).

Recently, Kohrt and Gomer (20) proposed the possible electronic interactions between adsorbed CO and tungsten (110) surface atoms on the basis of MO theory and the bond lengths:

a. bonding to a tungsten atom via the carbon atom: Interaction of C sp_z-orbital with the W d_z-orbital and the interaction of the CO π-MOs with the W d_{zy} and d_{zx} orbitals. If the "back donation" is sufficient this may not lead to electron deficiency for CO (See Figure 7a).

b. Bonding of carbon to 2 next nearest tungsten atoms via 2 sp_{yz}^2 C orbitals and d_{yz}-orbitals of the two W atoms. Bonding of C to 2 nearest W atoms does not seem possible because d-orbital density available for bonding is least along these directions.

c. Bonding of carbon to 2 next nearest tungsten atoms by the interaction of the filled C sp_z orbital with the d_{yz} orbital of the W atoms.

d. A "lying down" configuration, i.e. $\begin{matrix} C{-}O \\ | \quad | \\ W{-}W \end{matrix}$, in which C and O interact

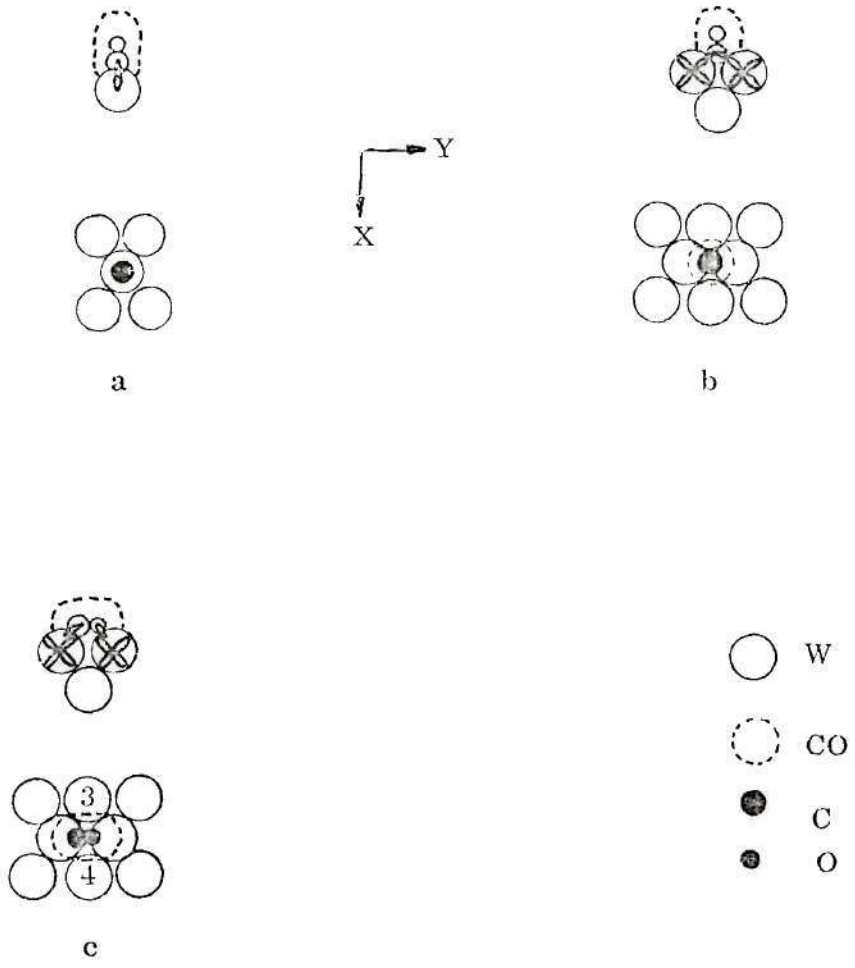

Figure 7. Schematic Representations (20) of Various Possible Binding Modes of CO on W (110) Surface. Upper Drawings Represent a Cross Section Cut Perpendicular to Surface and the Lower Drawings are Top Views. Dotted Lines Represent Van der Waal's Dimensions of CO.

with d_{yz} orbitals of next nearest W atoms via a C sp^2 and an O p or sp^2 orbital. In this configuration there will also be interaction of the CO MOs with the d_{xz} orbitals of the pair of 3rd nearest atoms (labelled 3 and 4 in Figure 7c).

1.4.2. Structure of Metal-Carbon Monoxide Bond in Chemisorption

The CO adsorbed on metals is known to be composed of a variety of chemisorption complexes. Infrared spectra studies by many investigators (21-27) have revealed two distinct species and related those to a linear structure $\overset{O}{\underset{M}{C}}$ and a bridged structure $\overset{O}{C}\!\!<\!\!\begin{matrix}M\\M\end{matrix}$. From thermal desorption studies it was concluded that the bridged structure is more strongly bound than linear species (28). The relative amounts of these two structures depend upon the metal as well as the nature of the support, if any (25). The presence of gaseous impurities in the metal can also have a marked effect on the relative amounts of bridged and linear structures (29). The strongly bound bridged structure requires greater donation of electrons from the metal; therefore impurities like hydrogen which donate electron to the metal will increase the amount of bridged structure, while impurities like oxygen which take away electrons from the metal decrease the relative amounts of bridged structure. It also has been noted that the bridged bond occurs when the distance between two nearest metal atoms on the surface is not greater than 2.6 Å (24, 30).

An additional infrared band observed for CO on nickel at higher pressure has been attributed to the linear structure on an already formed bridged species, namely, $\begin{matrix}Ni\!<\!\!\begin{matrix}CO\\CO\end{matrix}\\Ni\!<\!CO\end{matrix}$ (31). Other infrared bands observed for CO on unsupported

Ni films were attributed to linear and bridged species on different metal sites. The multiplicity of binding states has been reported for other metals also (21-24, 27, 32-34).

Another possible bridged structure of CO on metals is $\begin{matrix} C{-}O \\ | \quad | \\ M{-}M \end{matrix}$ (30, 35). Laynon and Trapnell (30) proposed this model and calculated that the optimum metal-metal distance for this structure is 3.25 Å. As was discussed in Sec. 1.3.1, Kohrt and Gomer (20) suggest this model for adsorption of CO on W(110) surface and the atoms assumed to take part in this structure are 3.16 Å apart.

Lynds (27) observed two band heads in the infrared spectra of CO adsorbed on ruthenium. These were attributed to a linear and a bridged species. Lynds (27) also suggested that this could be due to the same structure on two different kinds of sites. The infrared results of Kavtaradze and Sokolova (22-24) also supported the presence of linear and bridged carbon monoxide species. They also postulated that the bridged structure is formed at low coverage and at high coverage this may be converted to linear CO maintaining the equilibrium between the bridged and the linear species (22). Guerra and Schulman (21) observed two prominent band heads in the infrared spectra of CO on Ru and attributed these to the species Ru-CO (linear) and Ru_2-CO (bridged). Some additional band heads were attributed to more than one CO adsorbed on each protruding Ru atom.

1.4.3. Adsorption States of Chemisorbed Carbon Monoxide

Desorption experiments have been used by many workers (28, 18, 20, 15, 34, 36-42) to study the adsorption states of CO on metals. The results of those studies indicate that CO adsorbed on transition metals consists mainly of two

different states, α and β.

Flash-filament measurements on tungsten (28, 38, 39) have shown that there exist two different states of adsorbed CO. In these experiments CO was adsorbed on polycrystalline W filament and then the filament was heated to different temperatures as the pressure rise was recorded. One peak was formed at lower temperature (α) while three peaks (β_1, β_2 and β_3) were found close together at higher temperatures (23, 28). This showed that the CO in the α-state is loosely bound compared to that in the β-states. The β_1, β_2 and β_3 substates are strongly bound states in increasing order from β_1 to β_3. It was also observed that the population of α-state only becomes significant once the rate of uptake of CO in the β-states starts to decrease (36). Redhead (28) proposes that the α-state is due to the gap filling linear CO species; these gaps result from formation of the bridged CO species which corresponds to the β-states. The substates β_1 β_2 and β_3 are considered by Hill (38) to occupy different types of surface sites, characterized, for example, by the number of nearest neighbor atoms, adsorbing CO. Hill (38) also proposes that on W(113) surface CO molecules of the three substates form clusters. The break up of the clusters by evolution of the β-state would be followed by rehybridization of the remainder CO into more stable arrangements and similar thing occurs after β_2 is eliminated. Thus β_3-state is most strongly bound. α-state fills up the gap between the clusters.

Gomer and co-workers (36, 42) used field-emission techniques to measure the work function of several crystallographic faces of W at different coverages of CO. Thermal desorption was used to remove CO. In these experiments virgin,

α and β states of CO were identified. Physisorption may occur on the α-CO layer at a temperature between 27 and 30^{o}K (36). Virgin adsorption occurs at low temperatures (50^{o}K) and at higher temperatures initially β adsorption occurs after which α adsorption takes place. Gomer, et al (36, 42) suggested that in principle virgin adsorption was probably a similar process to that occurring at higher temperatures, but because of the low thermal energy involved a much more disordered structure results. The virgin phase appears to be stable up to 170^{o}K and above this temperature it desorbs partially the remainder being converted to β-CO.

The α-CO has a positive and the β-CO has a negative dipole moment (15, 36, 42). Measurements of $\Delta\phi$, combined with the abandance data show that the dipole moment of virgin CO (v-CO) is roughly 1.5 times that of β-CO (at 500^{o}K) (20).

Swanson and Gomer (15) have suggested an entirely speculative atomic scale model for the v-CO adsorption on W(100) surface (Figure 8). They suggested that at low temperature the adsorbed CO molecules do not have sufficient energy (thermal) to rearrange themselves into the lowest energy mode. They stay in an unactivated configuration (Figure 8a) which involves binding mainly via sp^2 hybridization of the carbon atom. This arrangement has a negative dipole moment. When the surface is heated to about 200^{o}K, the existing molecules "flip" into the more tightly bound locally situated β-configuration (Figure 8b). The temperature is high enough to activate such a process. This β-CO blocks further adsorption in any negative dipole state. Thus a positive (α) dipole state occurs on readsorption.

Kohrt and Gomer (20) propose two alternative atomic scale models for

a b

Figure 8. Schematic Representations (15) of Possible Configurations of CO Adsorbed on a W (100) Surface: a. Virgin Mode b. α and β States of CO.

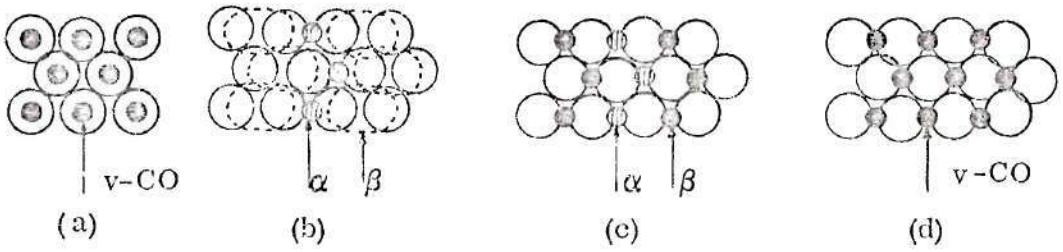

Figure 9. Schematic Representation of an Atomic Scale Model of Chemisorption of v, α and β-CO on W(110) Surface [According to Gomer et al (20)].

adsorption of CO on W(110) planes:

1. v-CO bonded to single tungsten atoms (Figure 9a): This would occur if bridged bonding requires appreciable distortion of the substrate lattice and an activation energy, or if the bridged bonding were weaker than bonding to single W atoms. The β-state in this case could be either CO bridged to two next nearest W atoms in "lying down" position (Figure 9b) or upright position (Figure 9c). In either case α-CO will correspond to the upright adsorption of CO via the carbon end between two free next nearest W atoms each of which is also bonded to a β-CO. Two kinds of adsorption, α and β, by bridged bonding (Figure 9c) can be explained by assuming that the d_{yz} orbital of a given W atom can be used only once (for β-bonding) and will not be available for the subsequent α-bonding. The negative dipole moment observed for v-CO can be explained by assuming sufficient back donation of electrons from d-orbitals to CO. The W atoms donate electrons to β-CO and β-CO has a negative dipole moment. It is assumed that α-CO is electron deficient because it interacts with W atoms which donated electrons to β-CO.

2. v-CO corresponds to bridge bonding (Figure 9d): If formation of the bridged structure requires no activation energy and is more stable than single atom bonding v-CO could take this form. In such a case, β-CO would be bridged to two next nearest W atoms in a "lying down" position and α-CO again is bridged to two next nearest W atoms each of which is bonded to a β-CO (Figure 9b). This model is also consistent with the observed dipole moments.

Both of these models can rationalize the observed virgin desorption/β

conversion behavior. By the first model, v-CO when desorbed at higher temperatures shifts to form β-CO either in lying down or upright position. Model 2 requires no displacement of the v-CO; v-CO automatically becomes α-CO when it is "flanked" by two β-CO. Thus v-CO can convert to $\alpha + \beta$ - CO without desorption. β-CO in the lying down configuration has a smaller dipole length than v-CO in upright configuration and so dipole moment of v-CO is more than that of β-CO.

From the work function measurements during thermal desorption experiments, Engel and Gomer (36) noted that the work function of W(100) and (110) surfaces goes below the clean value when CO adsorbed at 20^{o}K is desorbed above 850^{o}K (Figure 10). They suggested that this may be due to partial "burial" of CO still having a negative charge, the burial being due to rearrangement. If there were no rearrangement occurring, then there is more than one β configuration on these close packed planes. The α-state can be on "top of" a β layer even when no W atoms are directly available (36).

The regions which are atomically rough to start with seem to have only one β-state and there is little direct evidence of marked surface reconstruction or other anomalies although such events may simply be masked by the low work function of these planes when clean (36). The reconstruction occurs in close packed surfaces to increase the adsorbate substrate interactions.

Field-emission study of CO on tantalum (40) reveals three states of binding. The weakest state which corresponds to physisorption, desorbs at 125^{o}K. The second state is desorbed at above 650^{o}K, while the third state dissociates

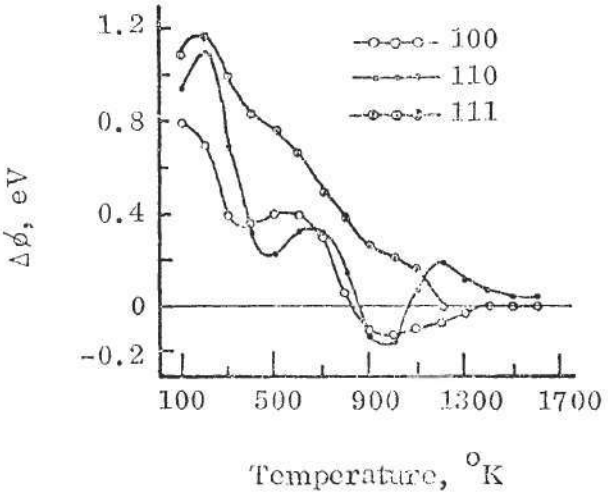

Figure 10. Plots of $\Delta\phi$ Versus 30-Second Heating Temperature for Full Virgin Layers of CO Deposited at 20°K (36).

before desorption to give an oxygen over tantalum pattern.

The α and β states are also reported on rhenium (37, 41) and ruthenium (41). Klein (41) reports that the two binding states of CO on ruthenium do not have sharp distinction between them. To identify the binding states he measured the voltage required to give a specified total field-emission current as a function of temperature of the ruthenium tip with an initial monolayer of CO. As pointed out in Sec. 1.2.3., this method does not reveal the changes in work function and thus may not be able to resolve the two states properly. The work function increment of ruthenium upon adsorption of CO was about 1.3 eV (the highest increment thus far reported for CO adsorption on metals) (41), which indicated very strong binding between CO and ruthenium. However, Klein (41) reported that most of the CO on ruthenium desorbed at less than 350^{o}K and the remaining amount desorbed by 500^{o}K; this indicated that most of the CO on ruthenium is weakly bound.

1.4.4. Surface Rearrangement upon Adsorption

When CO is adsorbed on a transition metal, it makes a chemical bond with the metal atoms on the substrate layer. As stated in Section 1.4.1, the CO admolecule competes for the d-electrons of the metal atoms. This may cause a weakening of the metal-metal bond in the substrate. This makes the movement of the atoms easier, and a reconstruction in the substrate layer which increases the substrate-adsorbate interactions may become possible. Since the interaction is less for unchanged atomically smooth planes, these planes have greater probability of reconstruction. The reconstruction may cause partial burial of some adsorbed molecules (36, 10).

Changes in the LEED pattern upon adsorption of CO on tungsten were interpreted to be due to surface reconstruction (34, 39). Field ion microscopy studies by Holscher (10) also supports the "corrosive" chemisorption. The high field used in the latter technique, however, could facilitate the reconstruction (36). Gomer, et al (36) attributed the decrease in ϕ below the value for clean surface during desorption of CO from tungsten to surface reconstruction of metal atoms upon adsorption.

Germer and McRae (43) formulated some guiding principles for reconstruction. When gas particles are held less strongly than the metal atoms in the reconstructed surface, the reconstruction should leave the number of missing metal-metal atoms unaltered. When the gas particles are held more strongly than the metal atoms, the reconstructed surface will have a maximum number of nearest neighbors even though the number of missing metal-metal nearest neighbors is increased.

The LEED studies have recently been interpreted by some workers (44-49) in terms of the structure of the adsorbed gases. From a compilation of data from LEED studies, Somorjai and Szalkowski (50) stated, "It appears that chemisorption leads to the formation of surface structures which exhibit maximal adsorbate-adsorbate and adsorbate-substrate interactions."

1.4.5. Surface Migration of the Adsorbed Carbon Monoxide

In many cases, it has been observed that the adsorbed particles migrate within the chemisorption layer. Surface migration is a thermally activated process and the migration occurs to sites where the bonding is stronger.

Klein (41) reports that migration of CO on ruthenium starts readily below 175°K, which indicates weak bonding between ruthenium and CO contrary to indications from the observed high $\Delta\phi_{ad}$ due to adsorption. Migration out of $\{11\bar{2}0\}$ type planes for ruthernium is very prominent while little migration is observed for CO on rhenium prior to desorption. Surface diffusion of CO on tungsten is observed at 275°K and higher temperatures (36) while migration of physisorbed and chemisorbed CO is observed at about 40 and 625°K, respectively, on tantalum adsorbates (40).

CHAPTER II

EXPERIMENTAL PROCEDURE

2.1. Materials

The ruthenium wires used in these studies were supplied by Engelhard Industries. Spectroscopic analysis by the supplier showed that the wire contained the impurities given in Table 1.

The original wire was 0.04 inch in diameter. The diameter was reduced to about 0.015 inch by electropolishing or by spark machining. Then the wire was annealed at about 700 to 800^{o}C for 2 to 3 hours under a vacuum better than 10^{-6} torr.

A typical analysis of the research grade carbon monoxide, as given by the Matheson Company, Inc. is given in Table 2.

2.2 Apparatus

Field-ion and Field-emission Microscope. The microscope was mounted on a Varian ultra-high vacuum system (model number 921-0034). The vacuum system was equipped with two vacsorb pumps, a titanium sublimation pump with a liquid nitrogen jacket, a 140 l/s ion pump and an automatic bake-out system. The microscope chamber which was attached to the vacuum system through a bakeable ultra-high vacuum valve had six ports to which other accessories could be attached. These accessories included a Varian partial pressure gauge tube,

Table 1. Ruthenium Wire Analysis

(All units in parts per million)

Pt 120	Pb 6	Mg 44	Mn 140	In -- not detected	Cd --not detected (limit of detection -- 50)
Rh 4	Sn 11	Ca 27	B 10	Zn --not detected	
Pd 4	Fe 1300	Al 180	Co 50	Sb -- not detected	Ru -- balance
Au 13	Cu 5 ext	Ni 180	Bi 2	As -- not detected	
Ag 2	Si 300	Cr 490	Ti 10	Mo -- not detected	

Table 2. Carbon Monoxide Gas Analysis

CO_2	less than	1 ppm
O_2		3 ppm
N_2		100 ppm
CO		Balance

two variable leak valves to which were connected one-litre pyrex flasks of research grade carbon monoxide and helium, and a high voltage feed-through. To mount the specimen inside the microscope chamber a glass specimen holder was used. Liquid nitrogen could be poured into the specimen holder for cryogenic cooling of the specimen. An earthed conducting fluorescent screen was mounted in front of the specimen position. The microscope chamber also contained a liquid nitrogen jacket surrounding the specimen holder.

Stabilized high voltage power supplies of 0-30 KV and 0-3 KV were used for applying voltage during field-ionization and field-emission microscopy, respectively.

A spot photometer (Gamma Scientific Inc., Model 2000, serial 135) was used to measure emission intensity during field-emission microscopy.

2.3. Specimen Preparation

The ruthenium wire of approximately 0.5 inch length and 0.015 inch diameter was spot welded to a tungsten loop. The loop then was mounted on a U-shaped holder for electropolishing. The tip of the specimen was coated with a lacquer.

The electropolishing was done in 5-10% KOH solution at about 24^{o}C. A ruthenium wire was used as counter electrode. An A.C. voltage ranging from 7 volts initially to about 0.8 volt during final polishing was used. During electropolishing the lower part of the specimen was manually moved in and out of the polishing solution with careful smooth cycles. Occasionally the specimen was

removed and observed under 360x magnification in an optical microscope. The established polishing sequence is illustrated in Figure 11. The dissolution occurs preferentially just above the lacquer coating resulting in a neck being formed. When the neck becomes prominent as shown in Figure 11c, the lacquer coating was washed away with acetone to avoid overloading of the neck. As the polishing continued the voltage was brought down in steps to about 2 volts. When the neck became extremely fine, as shown in Figure 11d, the voltage was brought down to about 0.8 volt. The polishing was continued at this voltage until the end below the neck dropped. Thus a fine tip was formed. The tip was observed with the optical microscope. The tip was brought in and out of focus to observe the discontinuity of the Fresnel fringes at the end of the tip (Figure 11e). The discontinuity showed that the tip was fine enough to be imaged in FIM. When the fringes were observed to be continuous, the specimen was not good and the polishing procedure was repeated.

After the specimen was satisfactorily electropolished it was washed with water and then with acetone. The specimen was now ready for the microscope.

2.4. Operation of the Field-Ion/-Emission Microscope

The tungsten loop with the electropolished specimen was mounted on the specimen holder of the microscope. The fluorescent screen was then replaced on the microscope. The vacsorb pumps were used to evacuate the system to a pressure in the micron range. The valve to the vacsorb pumps was closed and the ion pump and the titanium sublimation pump were used to evatuate the system

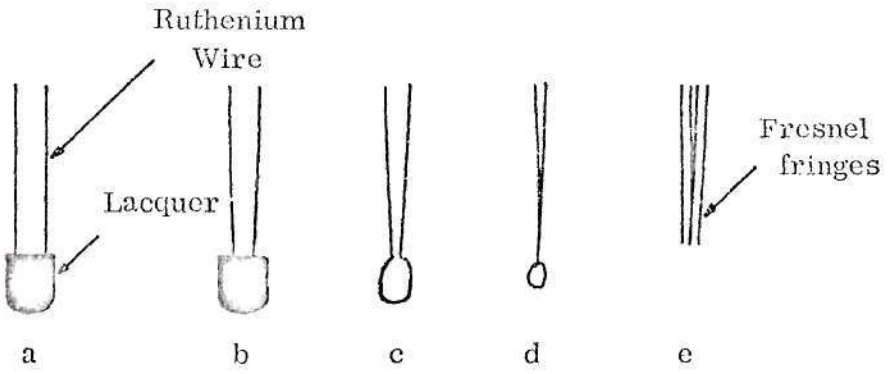

Figure 11. Stages of Electropolishing of Specimen for Field-Ion/-Emission Microscopy; (a) Before polishing, (e) At the End of the Polishing Sequence.

to the 10^{-7} torr range. The system was then baked at 250°C for 10 to 40 hours. The pressure was not allowed to exceed 4×10^{-6} torr during the bake-out. After the assembly cooled to room temperature and the pressure was 10^{-9} torr, the specimen was heated by passing in A.C. current through the tungsten loop. This was done to get rid of any corrosion products from the shank of the specimen. The pressure in the chamber went down to the 10^{-10} torr range in about 20 hours. Liquid nitrogen was poured in the jacket of the microscope chamber to reduce the pressure to the 10^{-11} torr range. Liquid nitrogen was then poured into the specimen holder. The liquid nitrogen temperat ure (77°K) was maintained throughout the experiment.

The ion pump valve was closed and helium admitted to a pressure of 10^{-4} torr. A positive voltage was then applied to image and field evaporate the specimen. After a certain extent of field evaporation the regular field-ion image was developed. When the regular image filled the screen, it was assumed that the specimen was smooth and round. A typical field-ion image of ruthenium is shown in Figure 12 to illustrate the perfection of the surface on which subsequent experiments were performed. The poles were indexed by the method developed by Newman, Sanwald and Hren (54).

With the high voltage still on, the helium gas was evacuated from the chamber with the ion pump. When the pressure was in the 10^{-9} torr range the voltage was brought down to zero. Now the specimen was connected to the negative terminal of the 0-3 KV supply. By slowly increasing the negative potential the field-emission image was obtained on the screen. The emission pattern showed

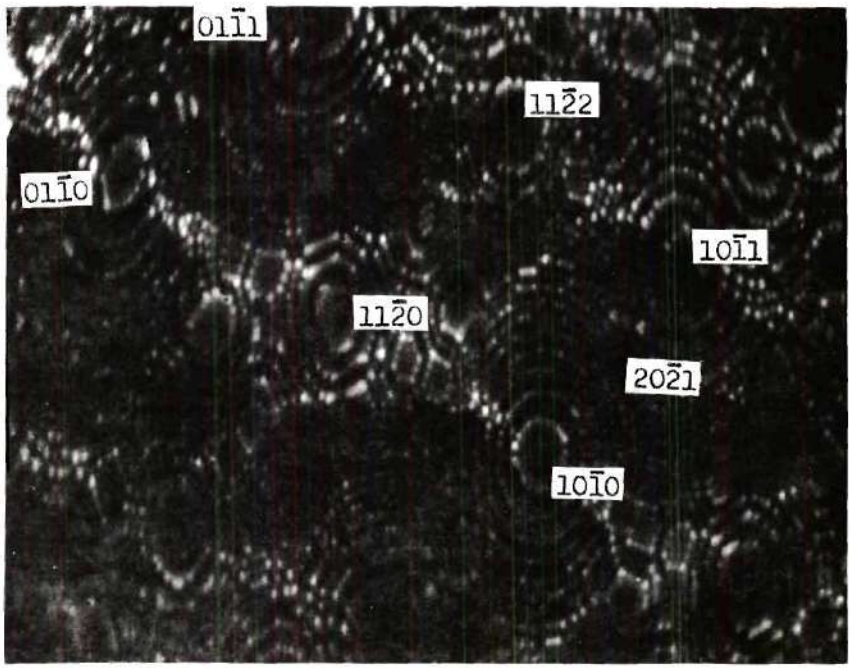

Figure 12. Field-Ion Micrograph of Ruthenium, 16 KV, 77°K, Helium Imaging Gas

that the specimen was not clean. This is due to gases, such as O_2, H_2O and CO_2, coming from the ion pump due to helium-ion bombardment; these gases contaminate the specimen. Field evaporation was then performed in a vacuum of approximately 10^{-11} torr. The applied voltage for evaporation in vacuum was 20 - 30% higher than that applied for evaporation in helium. After field evaporation, the field-emission pattern was again observed. This process of field evaporation and field emission was continued, increasing the evaporation voltage each time, until the field-emission pattern looked "clean." The intensity of emission in each area of the fluorescent screen was measured with the spot photometer as a function of the applied voltage. The applied emission voltages ranged from the minimum field-emission potential up to about 10% above this potential. The work function of the surface could then be calculated from this Fowler-Nordheim data by the method given in the Appendix. The evaporation field was then increased by about 0.25 KV and again the work function was measured. This was continued until the subsequent work function was constant. The field-emission pattern now obtained was considered clean. The indexing of field-emission patterns is similar to that of the field-ion images.

Work function measurements were made on the $(10\bar{1}1)$, $(10\bar{1}0)$, $(11\bar{2}2)$ and $(20\bar{2}1)$ regions. After the F-N data for a given region was obtained, the specimen was field evaporated again so as to expose a fresh surface for the measurement on another region.

Adsorption Studies. After the specimen was cleaned, carbon monoxide was introduced through the leak valve. The emission pattern was photographed at

approximately 3 second intervals.

Desorption Studies. After cleaning the specimen the F-N data were recorded for a given region and the specimen was again cleaned after which carbon monoxide was flowed through the microscope chamber at about 1.5×10^{-8} torr for about 15 seconds. A positive potential from zero to approximately 2 KV above the initial cleaning potential was applied in steps to desorb the CO. After each stage of desorption, F-N data were recorded for the selected region. Desorption studies were carried out for the $(10\bar{1}1)$, $(10\bar{1}0)$, $(11\bar{2}2)$ and $(20\bar{2}1)$ regions.

CHAPTER III

RESULTS

3.1. Work Functions for Single Crystal Regions of Ruthenium

The ruthenium field emitter was cleaned by field evaporation in a vacuum of 8×10^{-11} torr. The field-emission image was obtained and Fowler-Nordheim data was recorded for a given single crystal region. After each set of F-N data was obtained for one region the emitter was field evaporated to clean the surface for the next set of data. Except for the $(11\bar{2}1)$ region, more than one set of F-N data was recorded for each region.

Figure 13a shows a typical field-emission image of ruthenium. The work function of Ru $(10\bar{1}0)$ was reported to be $5.14 \pm .05$ eV by Savitsekii et al (53) this value was used to calculate the work functions of the other regions from the respective slopes of the Fowler-Nordheim plots as described in the Appendix. These results are given in Table 3.

3.2. Adsorption of Carbon Monoxide on Ruthenium

The ruthenium emitter was cleaned by field evaporation in a vacuum of 1.4×10^{-10} torr and 77^{o}K. Carbon monoxide was then introduced at a pressure of 2×10^{-9} torr. Micrographs of the emission patterns, shown in Figure 13, were taken while adsorption of CO was occurring on the ruthenium emitter.

Since the intensity of a given region changes during adsorption the following analysis of the micrographs can be made. During adsorption of CO on ruthenium

Table 3. Work Functions for Single Crystal Regions of Ruthenium

Region	Work Function (eV)	Number of Measurements
$(10\bar{1}0)$	$5.14 \pm .05$	4
$(10\bar{1}1)$	$5.01 \pm .06$	2
$(11\bar{2}2)$	$3.80 \pm .15$	4
$(20\bar{2}1)$	$4.51 \pm .15$	2
$(11\bar{2}1)$	$4.55 \pm .05$	1

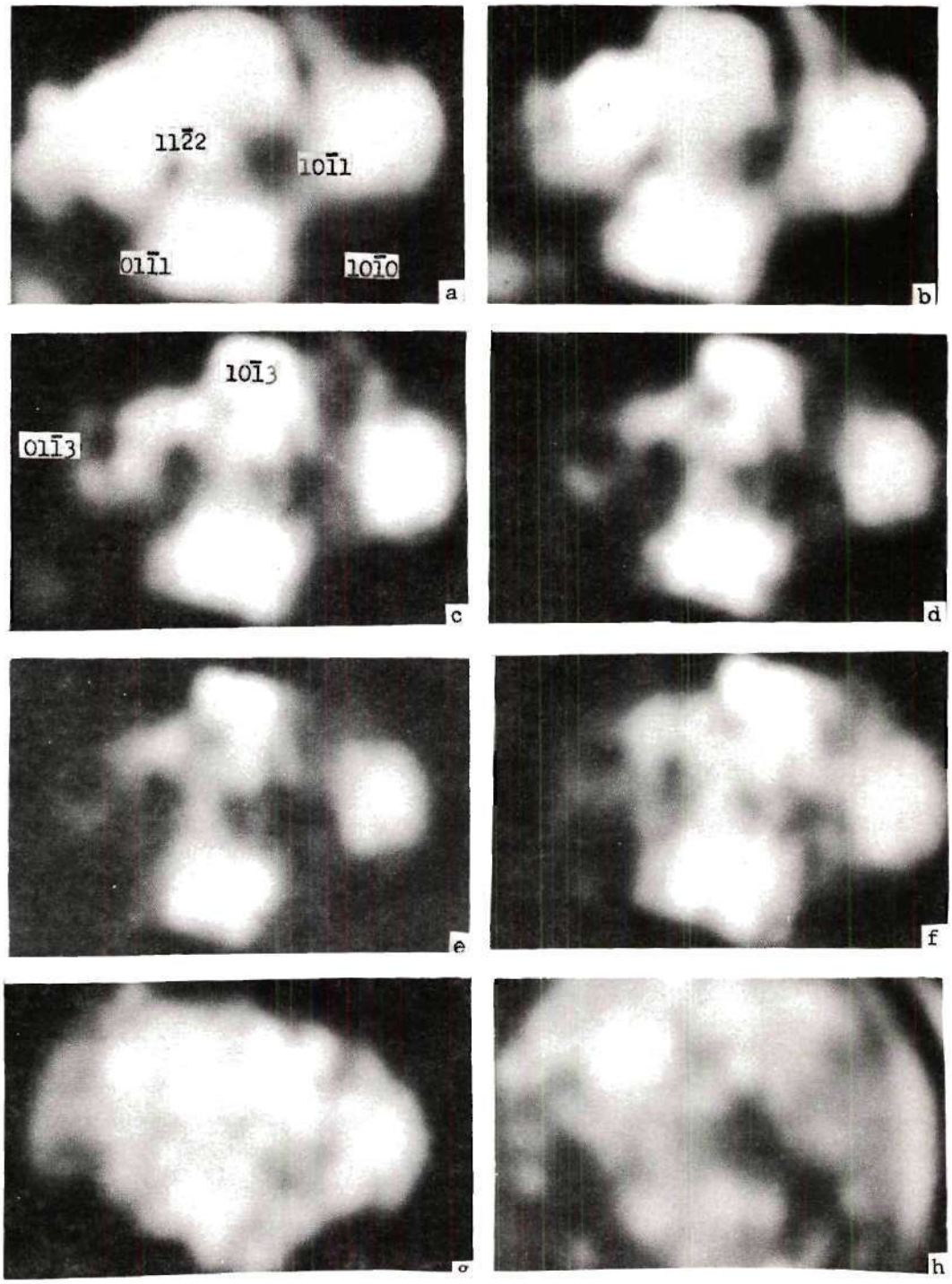

Figure 13. Field-Emission Micrographs of Ruthenium upon Adsorption of Carbon Monoxide at a Pressure of 2×10^{-9} Torr: (a) clean Ruthenium (Vc = 25.4 KV); Exposed to CO (b) 3 Seconds, (c) 6 Sec., (d) 9 Sec., (e) 12 Sec., (f) 15 Sec., (g) 18 Sec., (h) 60 Sec.

the total intensity appeared to decrease indicating some adsorption over the entire surface. However the rate of adsorption and/or the nature of interaction varies from region to region. Thus the $\{10\bar{1}3\}$ regions become less emitting compared to the surrounding regions as shown in Figure 13b. The $\{10\bar{1}3\}$ regions grow as the time of adsorption increases, as seen in the Figures 13b-e. The micrographs in these figures also show that adsorption occurs initially near the edges of the $\{10\bar{1}1\}$ planes and then spreads towards the $\{11\bar{2}2\}$ regions. The $\{11\bar{2}2\}$ regions appear darker than the surrounding regions in the initially clean pattern and in subsequent patterns up to 6 seconds exposure to CO. However, after 9 seconds emission from the $\{11\bar{2}2\}$ regions becomes more intense than that from the surrounding regions. This is due either to more adsorption on the surrounding regions or to a difference in adsorption states.

The $\{10\bar{1}1\}$ regions which appear dark in the clean emission pattern remain dark during adsorption but their relative intensity increases. This shows that either the extent of adsorption or the degree of interaction of CO on the $\{10\bar{1}1\}$ regions is less than that on the surrounding regions.

After approximately 60 seconds further adsorption, if any, it does not seem to change the total intensity or the intensity anisotropy of the emission pattern. This is subsequently referred to as saturated adsorption. Figure 13h, which was taken from a series on another specimen, shows a typical micrograph after saturated adsorption.

3.3. Field Desorption of Carbon Monoxide from Ruthenium

After cleaning the emitter by field evaporation at a pressure below 5×10^{-10}

torr the specimen was exposed to CO at 1.5×10^{-8} torr for about 15 seconds. From the above results this can be assumed to be adequate for saturated adsorption. The emission patterns before and after adsorption are shown in Figures 14a and 14b, respectively. From these micrographs it can be seen that the emitting area increased due to CO adsorption. While the emitting area in Figure 14a had been cleaned by field evaporation the additional emitting area in Figure 14b had probably not been cleaned entirely of oxide or other surface film. These results indicate that CO adsorption either decreased the emission from clean ruthenium more than that from the adjacent film or else increased the emission of the unclean regions. This may be due to more CO adsorption on clean ruthenium or to different types of adsorption on clean ruthenium and on the surface film. After saturated adsorption was obtained the system was evacuated to below 8×10^{-10} torr.

a. Field emission patterns during desorption: A positive voltage was applied to field desorb CO from ruthenium. After desorption at a given field for about 50 seconds the field was reversed and the emission pattern was recorded. A series of micrographs showing the emission patterns after field desorption are given in Figures 14c-h. The voltage applied for field desorption is reported in percent of the field evaporation voltage of the initially clean specimen (percent Vc). From these figures it can be seen that at desorption fields below about 78% Vc neither the relative intensity of the different regions of the emitter nor the total intensity change to a great extent. Above 78.5% Vc, however, the overall intensity of emission starts increasing (note the reduction in exposure time in Figures 14c and d.). The emission intensity becomes so high beyond

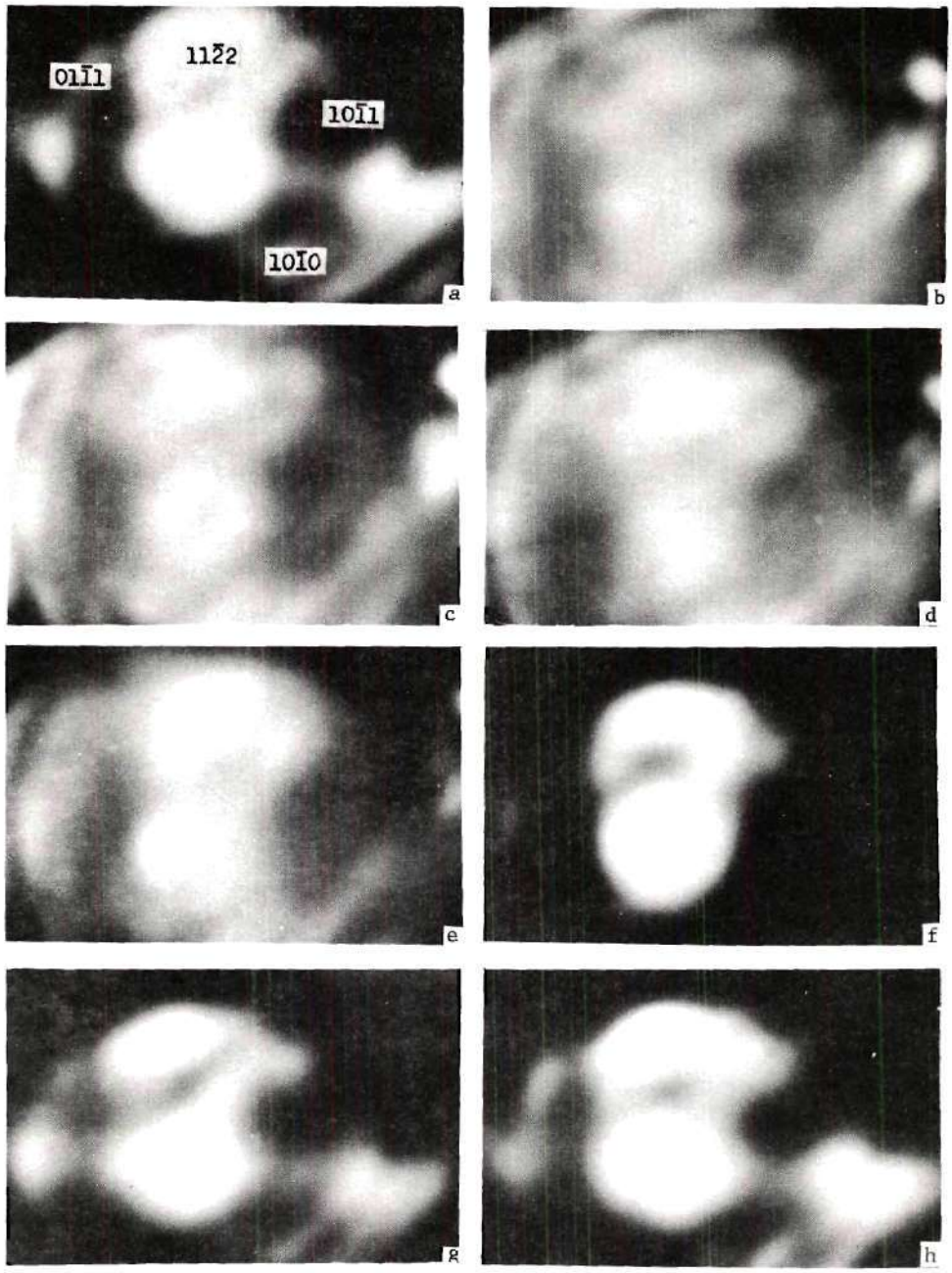

Figure 14. Field-Emission Micrographs of Ruthenium Specimen during Desorption of Carbon Monoxide, the FEM Potentials and Photographic Exposure Times Are Given in Parenthesis: (a) Clean (Vc = 29.5 KV) (-2KV, ½ Second), (b) CO adsorbed for 15 Seconds at 1.5 x 10^{-8} Torr (-2.99 KV, 65 Sec.), (c) Desorption at 78.5% Vc (-2.99 KV, 30 Sec.), (d) Desorption at 91.6% Vc (-2.99 KV, 10 Sec.), (e) Desorption at 93.5% Vc (-2.9 KV, 20 Sec.), (f) Desorption at 95% Vc (-1.99 KV, ½ Sec.), (g) Desorption at 96.4% Vc (-2 KV, ½ Sec.), (h) Desorption at 101% Vc (-2 KV, ½ Sec.)

93.5% Vc that the emission potential had to be progressively decreased (Figure 14e-f). The relative intensity of the low index regions, compared to that of surrounding high index regions is greater at 91.6% than at 78.5% Vc (Figure 14d). At about 93.5% Vc the portion near the apex of the tip becomes more highly emitting than other regions of the specimen, probably due to the higher field near the apex giving rise to earlier desorption. At 95% Vc only this portion of the tip is observed at the lower emission voltage applied (Figure 14f). At 96.4% Vc the emission pattern looks similar to the original pattern before adsorption. The small observable difference is that the relative intensity of the dark low index regions is slightly less in the pattern of the clean specimen. When a desorption potential above 100% Vc is applied the emission pattern (Figure 14h) is not noticeably different from that before adsorption.

b. Fowler-Nordheim plots for single crystal regions during desorption: In these experiments Fowler-Nordheim data were recorded for a given crystallographic region at each stage of the desorption sequence described above. Several measurements were made on the $(10\bar{1}0)$ and $(10\bar{1}1)$ regions and one measurement each on the $(11\bar{2}2)$ and $(20\bar{2}1)$ regions. From these Fowler-Nordheim data, work functions (ϕ), pre-exponential factors (A) and emission voltages (V) for a specified constant emission were calculated. The $\Delta\phi_{ad}$, $\Delta(\ln A)_{ad}$, and V_{ad}/V_{cl} values were then plotted against the desorption potential in percent Vc, where

$$\Delta\phi_{ad} = \phi_{ad} - \phi_{cl} \qquad (13)$$

$$\Delta(\ln A)_{ad} = (\ln A)_{ad} - (\ln A)_{cl} \qquad (14)$$

and V_{ad}/V_{cl} = ratio of emission voltage of specimen with adsorbed CO (V_{ad}) to that of the clean specimen (V_{cl}) for constant emission. Examples of these plots for each crystal region are shown in Figures 15-18.

For each of these regions the voltage for constant emission increases upon adsorption. During desorption from the $(10\bar{1}1)$ and $(10\bar{1}0)$ regions the emission voltage (V_{ad}) does not change much until about 79% Vc where there is a slight decrease in V_{ad} and this is followed by a small increase in the case of the $(10\bar{1}1)$ region. This small decrease and increase in V_{ad} are absent for the $(11\bar{2}2)$ and $(20\bar{2}1)$ regions. There is a large decrease in V_{ad} for each of these regions with the minima at 92.6%, 92.2%, 89.6% and 90.9% Vc, respectively.

For each of these regions the work function also increases upon adsorption while the pre-exponential factor decreases, as shown by the $\Delta\phi_{ad}$ and $\Delta(\ln A)_{ad}$ values, respectively, at 0% Vc. During desorption of CO, the changes in ln A follows closely the changes in ϕ (with the possible exception of the $(20\bar{2}1)$); that is, an increase or decrease in ϕ is accompanied by an increase or decrease, respectively, in ln A. For the $(10\bar{1}1)$ region (Figure 15), there is a small increase in ϕ initially during desorption of CO. Then there is a decrease (desorption stage I) in ϕ with a minimum at 79% Vc and a subsequent increase (II) to a maximum at 86.8% Vc. Similar $\Delta\phi$ changes occur for the $(10\bar{1}0)$ region (Figure 16). The desorption stage II is absent for the $(11\bar{2}2)$ and $(20\bar{2}1)$ regions (Figures 17 and 18, respectively). For all the regions the desorption stage III leads to a negative $\Delta\phi_{ad}$.

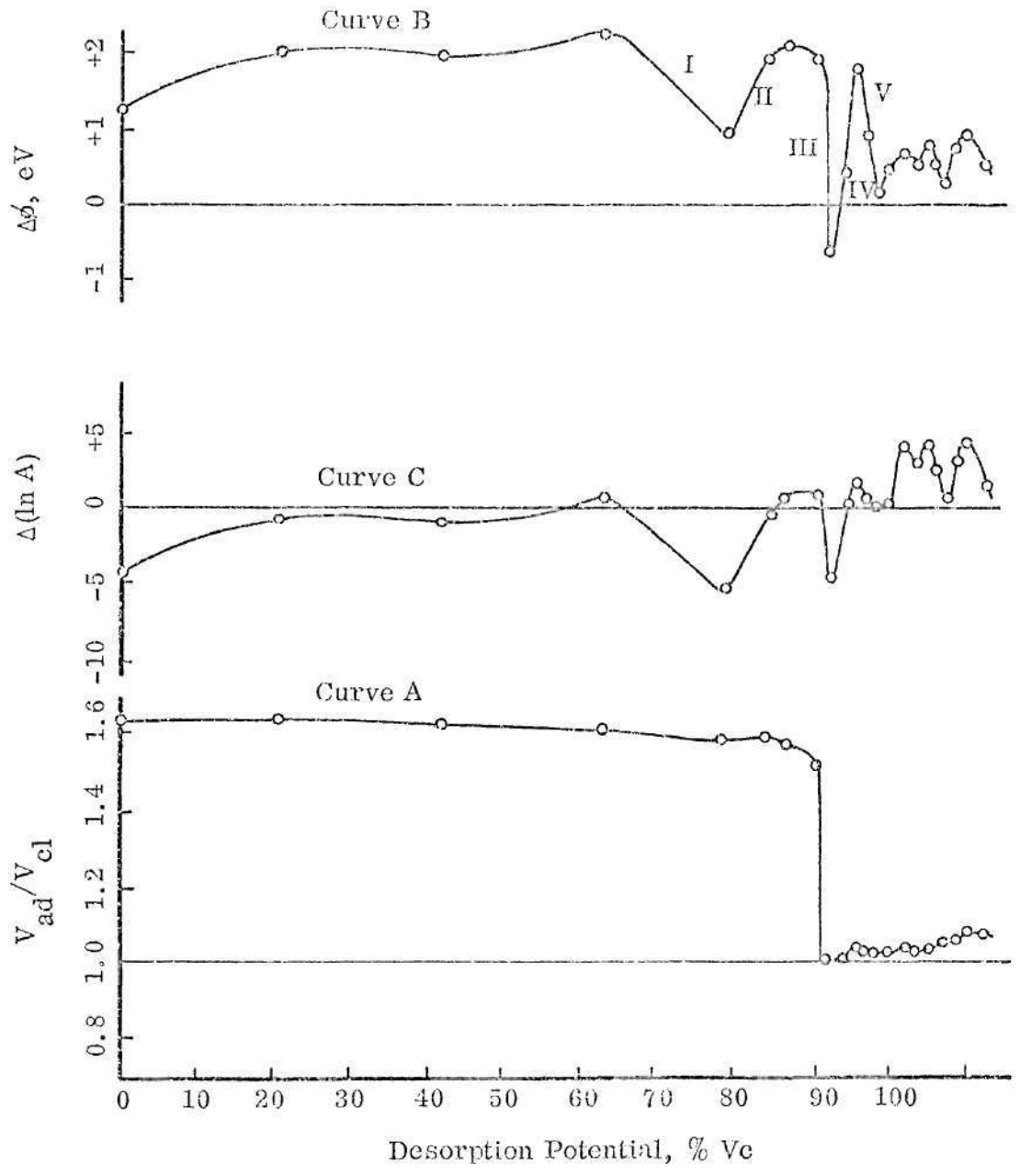

Figure 15. Carbon Monoxide Desorption from the $(10\bar{1}1)$ Region of Ruthenium: Plots of V_{ad}/V_{cl} (Curve A), $\Delta\phi_{ad}$ (Curve B) and $\Delta(\ln A)_{ad}$ (Curve C) Versus Desorption Potential; $\phi_{cl} = 5.01$ eV, $\ln A_{cl} = 23.31$ and $V_{cl} = -1.35$ KV.

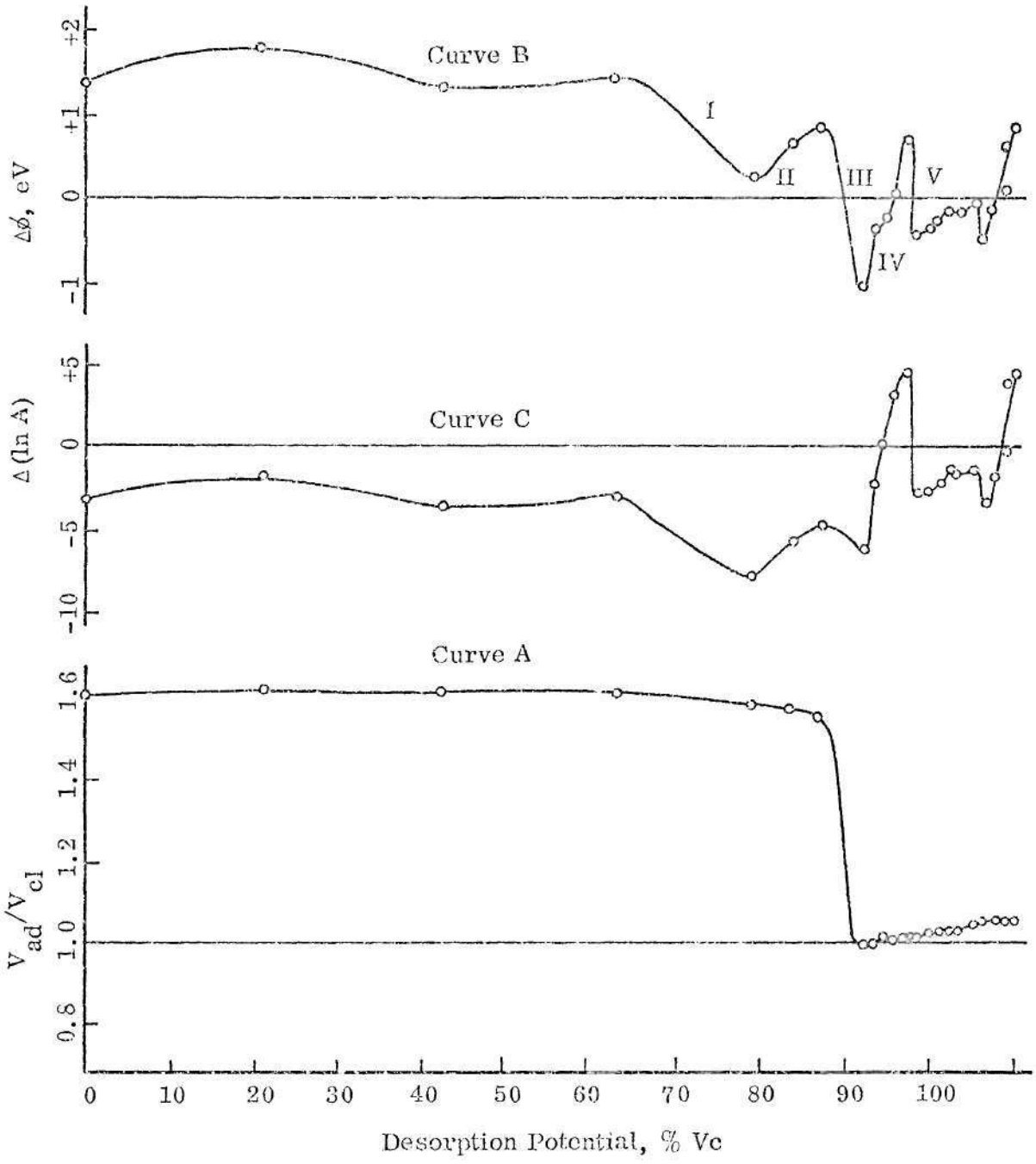

Figure 16. Carbon Monoxide Desorption from the $(10\bar{1}0)$ Region of Ruthenium: Plots of V_{ad}/V_{cl} (Curve A), $\Delta\phi_{ad}$ (Curve B) and $\Delta(\ln A)_{ad}$ (Curve C) Versus Desorption Potential; $\phi_{cl} = 5.14$ eV, $\ln A_{cl} = 22.29$ and $V_{cl} = -1.53$ KV.

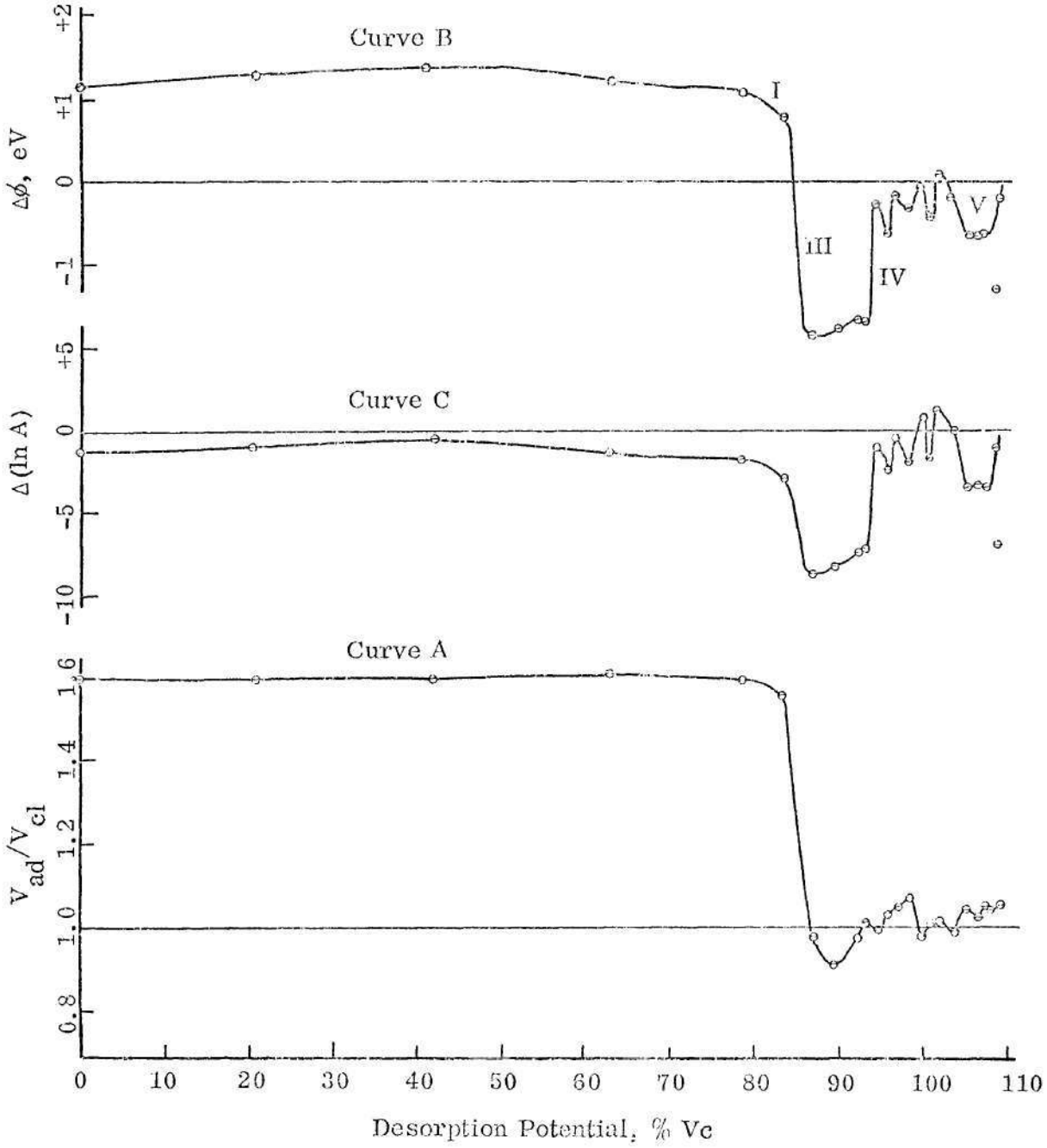

Figure 17. Carbon Monoxide Desorption from the $(11\bar{2}2)$ Region of Ruthenium: Plots of V_{ad}/V_{cl} (Curve A), $\Delta\phi_{ad}$ (Curve B) and $\Delta(\ln A)_{ad}$ (Curve C) Versus Desorption Potential, $\phi_{cl} = 3.80$ eV, $\ln A_{cl} = 16.0$ and $V_{cl} = -1.86$ KV.

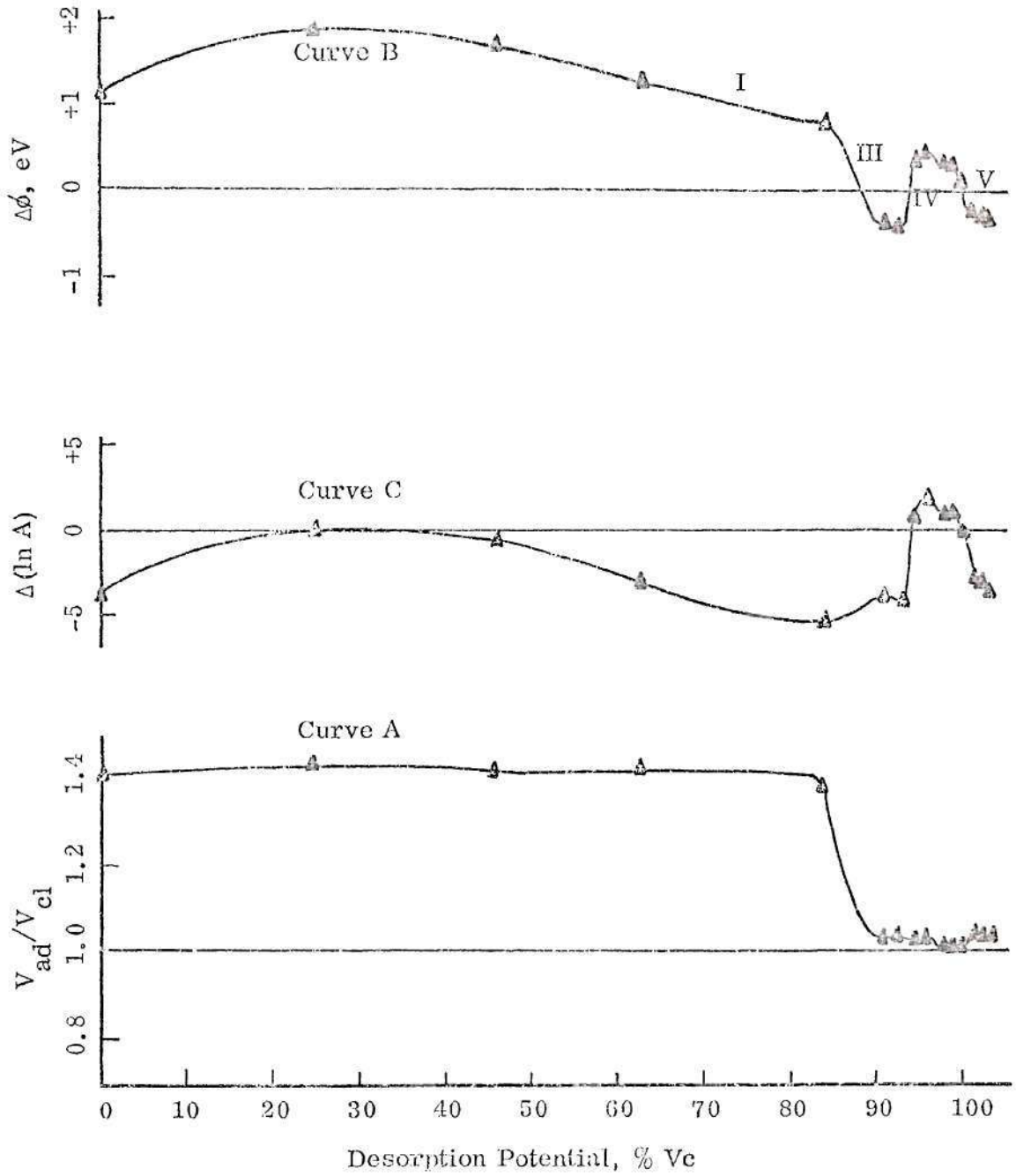

Figure 18. Carbon Monoxide Desorption from the $(20\bar{2}1)$ Region of Ruthenium: Plots of V_{ad}/V_{cl} (Curve A), $\Delta\phi_{ad}$ (Curve B) and $\Delta(\ln A)_{ad}$ (Curve C) Versus Desorption Potential; $\phi_{cl} = 4.51$ eV, $\ln A_{cl} = 21.0$ and $V_{cl} = -2$ KV.

For a given crystal region on different specimens the desorption stages I-V and the corresponding $\Delta\phi$ minima and maxima do not occur at the same desorption potential. In Figures 19 and 20 for the $(10\bar{1}1)$ and $(10\bar{1}0)$ regions, respectively, the desorption potential coordinates have been adjusted so that the desorption potentials for the ϕ minima corresponding to the large emission drop for each specimen coincide. This large drop in emission indicates removal of the major chemisorption state. The similarities of the desorption process for a given region on different specimens can then be seen in these "normalized" curves; that is, the major maxima and minima in work function changes overlap throughout the desorption spectra. The magnitude of the $\Delta\phi$ associated with each stage varies to some extent, but certain trends are observed in these values. The reason for differences in the desorption potential of a given state and the corresponding $\Delta\phi$ values are discussed in Chapter IV (Section 4.5). Table 4 summarizes the important desorption stages and the corresponding ϕ changes for the observed maxima and minima during desorption of CO from the $(10\bar{1}1)$, $(10\bar{1}0)$ $(11\bar{2}2)$ and $(10\bar{2}1)$ regions of ruthenium. The $\Delta\phi$ values given in this table are the differences in the ϕ before and after a given desorption stage.

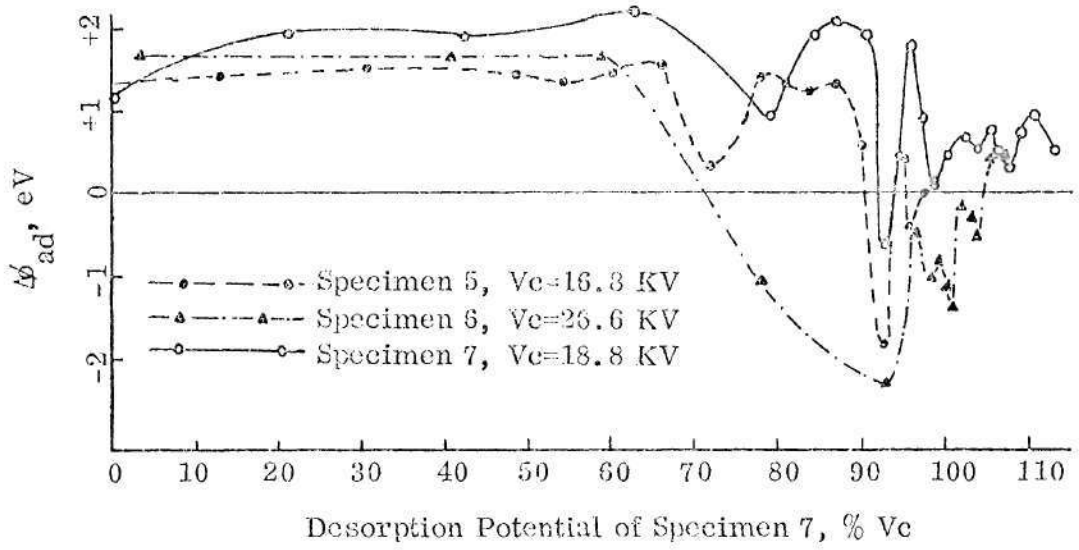

Figure 19. Carbon Monoxide Desorption from the Ruthenium (10$\bar{1}$1) Regions on Specimens 5, 6 and 7: Plots of $\Delta\phi_{ad}$ Versus "Normalized" Desorption Potential.

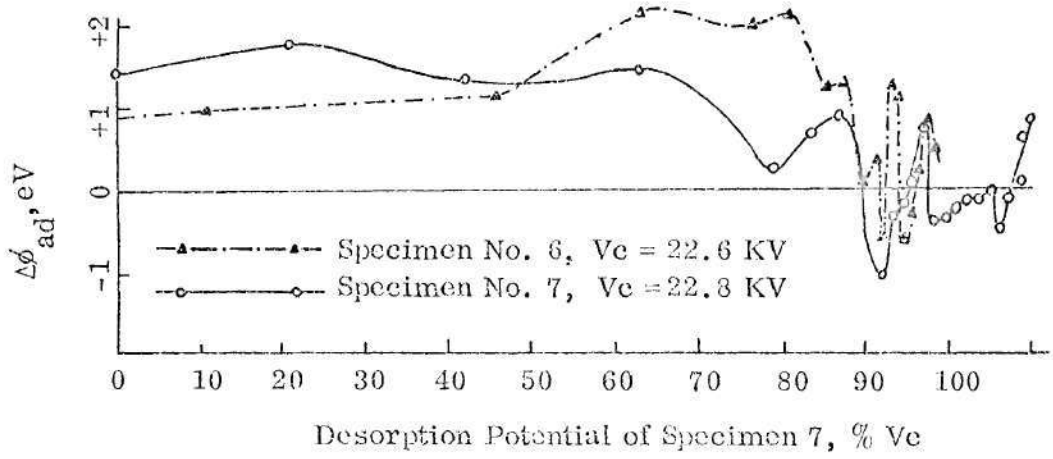

Figure 20. Carbon Monoxide Desorption from the Ruthenium (10$\bar{1}$0) Regions on Specimens 6 and 7: Plots of $\Delta\phi_{ad}$ Versus "Normalized" Desorption Potential.

Table 4. Changes in Work Function (eV) During Field Desorption of Carbon Monoxide from Ruthenium and Desorption Potential of Corresponding Maxima and Minima

Region	Specimen Number	Vc (KV)	$\Delta\phi_{ad}$ (at 0% Vc)	Desorption Stage I		Desorption Stage II		Desorption Stage III		Desorption Stage IV		Desorption Stage V	
				% Vc	$\Delta\phi$	% Vc	$\Delta\phi$	% Vc	$\Delta\phi$	%Vc	$\Delta\phi$	% Vc	$\Delta\phi$
	5	16.8	+ 1.32	76.9	-1.27	82.8	+1.08	97.6	-3.19	100	+2.24	101	-0.9
$10\bar{1}1$	6	26.6	+ 1.72					89.6	-3.99	93.3	+1.81	97.8	-0.95
	7	18.8	+ 1.21	79	-1.28	86.8	+1.15	92.6	-2.55	96	+2.43	98.7	-1.65
	4	22.8		79	-0.98	85.5	+0.6						
$10\bar{1}0$	6	22.6	+ 0.86					99.2	-1.87	100	+1.87	102	-1.94
	7	22.8	+ 1.4	79.1	-1.18	87	+0.62	92.2	-1.93	97.4	+1.75	98.7	-1.1
$11\bar{2}2$	8	26.8	+ 1.22	83.7	-0.61			87	-2.64	94.8	+1.4	105	-0.7
$20\bar{2}1$	6	28.4	+ 1.09	83.9	-1.11			92.7	-1.19	95.8	+0.86	103	-0.8

CHAPTER IV

DISCUSSION

4.1. Adsorption States of Carbon Monoxide on Ruthenium

The work function on each plane increases to a large extent upon adsorption. This shows that the net surface potential of the adsorbed carbon monoxide on ruthenium is negative. However, this net negative surface potential arises due to presence of a mixture of species having positive and negative dipole moments. From the field desorption results (Figures 15-18) the following analysis can be made about the nature of the adsorbed states.

Initially during desorption there is a slow increase in ϕ, showing that the species being desorbed has a small positive dipole moment. This corresponds to the removal of physisorbed CO, which is weakly bound and thus desorbed at low fields.

The desorption stage I can be explained as a rearrangement process. The application of a field may activate rearrangements of the metal atoms in the substrate layer and/or rearrangements of the adsorbed CO molecules in the adsorbate layer. Either of these will occur to increase the substrate-adsorbate interactions. If the adsorbate layer rearranges, then this may cause an increase in the surface potential depending upon the nature of the rearrangements. If the substrate layer rearranges, this may cause a burial of the adsorbed CO with a negative dipole moment (36). This again will increase the surface potential. The rearrangements

of the substrate and/or the adsorbate layer thus cause a decrease in ϕ corresponding to desorption state I in the desorption spectra. Rearrangements were found to occur on each of the regions investigated.

The desorption stage II for the $(10\bar{1}1)$ and $(10\bar{1}0)$ regions, which is characterized by an increase in ϕ, corresponds to the removal of an electropositively bound species. This CO species having a positive dipole moment is the α-state. The desorption stage II was not observed for the $(11\bar{2}2)$ and $(20\bar{2}1)$ regions, which indicates the absence of the α-state on these regions. The small decrease in emission from the $\{10\bar{1}0\}$ and $\{10\bar{1}1\}$ regions in Figure 14e may be attributed to desorption of the α-state. The change in $\Delta\phi_{ad}$ value during desorption of α-CO from the $(10\bar{1}1)$ region is greater than that for the $(10\bar{1}0)$ region (Table 4) indicating stronger interaction and/or a larger quantity of the adsorbed α-state on the $(10\bar{1}1)$ region than on the $(10\bar{1}0)$ region.

The desorption stage III corresponds to the removal of an electro-negative species or β-state of CO. The β-CO was observed on all the regions investigated and the decrease in emission voltage in Figure 14f is attributed to the desorption of the β-state. The changes in $\Delta\phi_{ad}$ values during desorption of β-CO from ruthenium decreases in the order of $(10\bar{1}1)$, $(11\bar{2}2)$, $(10\bar{1}0)$ and $(20\bar{2}1)$ regions. This indicates that the extent of interaction and/or the amounts of adsorbed β-CO decreases in the same order. The observed work function minima below the values for the clean specimen after β desorption can be explained by the concept of "corrosive chemisorption" of CO (10) on ruthenium. The "corrosive chemisorption" changes the arrangement of the metal atoms in the substrate layer, and the CO

molecules which have a negative dipole moment are buried inside the metal surface. The protruding metal atoms exhibit a positive dipole moment. Therefore, when β-CO is desorbed the surface layer with buried CO is exposed and gives rise to a net positive surface potential and thus decreases the work function below that of the clean surface.

The desorption stage IV, which was also found on all regions, corresponds to desorption of the protruding metal atoms and thus exposure of the buried CO. The negative dipole moment of these CO molecules causes a rise in ϕ over the value of the clean surface. The desorption stage V represents the removal of the corrosive chemisorbed CO molecules from the surface. The oscillation of the ϕ value after desorption stage III indicates either the stepwise removal of a single corrosive chemisorbed layer or the existence of more than one of these layers.

The pre-exponential factor (A) decreases upon adsorption. As discussed in Chapter I (section 1.2.3), this is due to polarization of the adsorbed layer by the electrostatic field applied for emission. As the physisorbed layer is desorbed the ln A value increases (Figures 15-18). The ln A value decreases again when the surface reconstruction in desorption stage I occurs. As discussed in Section 1.2.3, ln A may decrease due to "corrosive chemisorption" resulting from reconstruction of the substrate. When α-CO is desorbed in desorption stage II, ln A again increases due to removal of adsorbed species. The decrease in ln A corresponding to β-CO desorption in desorption stage III cannot be explained satisfactorily. This decrease may be due to the exposure of the "demetallized" surface produced by "corrosive chemisorption."

The desorption stages are summarized in Table 5. From these results the following interpretations can be made about the adsorption states of CO on ruthenium. When CO is first adsorbed on ruthenium at 77°K, a virgin-CO is probably formed over the surface. The adsorption of CO *in a virgin state* does not lead to the best interaction between the substrate and adsorbate. For better interactions some rearrangement is necessary in the substrate and/or adsorbate layers. The activation energy necessary for such rearrangement may not be thermally supplied at 77°K and thus a virgin-CO layer is formed. Over the virgin layer a physiosorbed layer is formed. The physisorbed layer is desorbed at low fields. When the field is adequate to activate the rearrangements, the virgin-CO is converted to give a buried CO species ("corrosive chemisorbed") with β-CO and, in the case of the $(10\bar{1}1)$ and $(10\bar{1}0)$ regions, α-CO chemisorbed on the rearranged substrate. The electronegative β-CO is more strongly bound than the electropositive α-CO and therefore is desorbed at a higher field. When these states are desorbed, the rearranged substrate with "corrosive chemisorbed" CO is exposed. This CO is desorbed as the field is raised further.

4.2. Reconstruction of Metal Atoms in the Substrate Layer

The results of these studies strongly support the idea of reconstruction of the metal atoms discussed in Section 1.4.4. Some LEED studies (34, 39) of carbon monoxide on a tungsten surface show a well developed pattern different from the pattern of the clean tungsten surface. This was interpreted to support reconstruction of the substrate during adsorption. FEM results (36) have also been

Table 5. Interpretation of Desorption Stages of Carbon Monoxide on Ruthenium

Desorption Stage I	Rearrangements of the substrate and/or adsorbate.
Desorption Stage II	Desorption of electropositive α-state of carbon monoxide (found only on $(10\bar{1}0)$ and $(10\bar{1}1)$ regions).
Desorption Stage III	Desorption of electronegative β-state of carbon monoxide
Desorption Stage IV	Desorption of protruding metal atoms in rearranged layer exposing buried carbon monoxide.
Desorption Stage V	Desorption of the carbon monoxide exposed in desorption stage IV

interpreted as reconstruction during carbon monoxide adsorption on tungsten. Similar reconstruction may also be favorable for ruthenium substrates. Ruthenium has three empty 4d orbitals and therefore is expected to interact with CO quite strongly. The metal-metal bond in ruthenium is weaker than that in tungsten (heat of atomization of solid ruthenium and tungsten at 298^{o}K are 153 and 203 Kcal/gm-atom, respectively (55)) and thus it is expected that ruthenium atoms have a greater probability of reconstruction upon adsorption than tungsten atoms. At the present time it is not possible to speculate the nature of such reconstruction and estimate the activation energy of such process. However, this energy may be so high that thermal energy at 77^{o}K is not adequate and fast reconstruction is possible only when the specimen is heated to higher temperatures or an electrostatic field is applied.

The reconstruction may cause partial burial of CO molecules below ruthenium atoms on the surface thereby giving a positive surface potential. These molecules will be surrounded by ruthenium atoms and will be strongly bound.

Madey and Yates (55) used the thermionic retarding potential method to measure the work function changes during adsorption of CO on tungsten (110) and (100) surfaces. For the (110) surface they reported that an electropositive state populates rapidly on a warm surface, followed by an electronegative state as the surface cools to room temperature, while adsorption on the (110) surface initially cooled to room temperature is dominated by the electronegative state. These results are consistent with the concept of reconstruction upon adsorption when sufficient thermal energy is available. The reconstruction on a tungsten surface

needs a high activation energy. Thus reconstruction at room temperature is less compared to that occurring at high temperature. The reconstruction which causes partial burial of CO molecules yields a positive surface potential. After reconstruction and the burial of CO occurs β-CO is adsorbed. The β-CO has a negative dipole moment due to donation of electrons from the metal atoms and thus has a negative surface potential. The fast adsorption of the "electropositive state" actually may be an electronegative state buried under metal atoms. The reconstruction being faster at higher temperature, the apparent "electropositive state" populates rapidly on warm surface compared to the surface at room temperature. For the (100) surface Madey and Yates found that the ϕ value does not go below that for the clean surface. This indicates that reconstruction is negligible on this surface.

The concept of reconstruction of ruthenium substrate upon adsorption of CO can be checked only with LEED studies which will also give the details of the reconstructed surface.

4.3. Atomic Models for the Arrangements of Adsorbed Carbon Monoxide

If reconstruction actually occurs during formation of the α- and β-states, it will not be exact to speculate any model of carbon monoxide adsorption without knowing the reconstructed arrangements of the metal atoms. The reconstructed surface of ruthenium in the presence of CO is not known. However, an attempt is made here to show the influence of atomic scale geometry of the substrate layer on the nature of adsorption on the $(11\bar{2}2)$ and $(10\bar{1}1)$ regions. These models are

similar to that for CO on tungsten (110) surface, previously given by Gomer, et al (20). In the models below the reconstruction is neglected; therefore these models should not be considered exact. These models should not be considered exact also because the adsorption states were found on the regions and may not correspond to planes only. Steps on these regions may be contributing to observed adsorption states.

Before discussing the atomic models it is necessary to consider the shape of the CO molecule. The Van der Waals shape of the CO molecule is considered to be a cylinder of diameter of about 2.8 $\mathring{A}$ with hemispherical caps at both the ends. The overall length of the CO molecule is 4.1 $\mathring{A}$ (20).

4.3.1. $(11\bar{2}2)$ Surface

In these studies no α-CO was found on the $(11\bar{2}2)$ region of ruthenium. Thus the arrangement of CO on this surface is somewhat less complicated and will be considered first. Figure 21 shows the arrangement of β-CO on top of $(11\bar{2}2)$ planes. The CO molecules are assumed to be adsorbed in a lying down position. The dotted lines show the Van der Waals dimensions of CO. Gomer, et al. (20) suggested that CO in the lying down position on tungsten may be most strongly bound (Sections 1.4.1 and 1.4.3). If the interaction is greater on the carbon end of CO, then the carbon end will be on the outermost ruthenium atoms, as shown in Figure 21. If whole surface is almost covered by CO molecules in the lying down position and there is no space available for additional CO molecules to come directly in contact with the metal atoms, any further CO getting adsorbed must then be "physisorbed." The β-CO in a lying down position would have a large negative dipole moment and

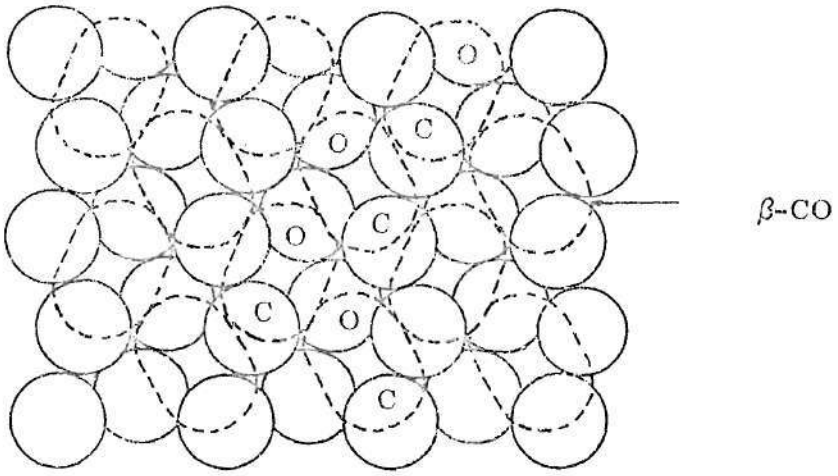

Figure 21. Carbon Monoxide on Ruthenium $(11\bar{2}2)$ Surface.

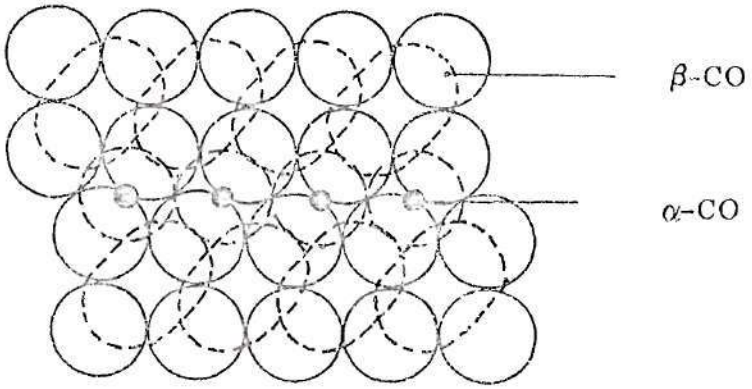

Figure 22. Carbon Monoxide on Ruthenium $(10\bar{1}1)$ Surface.

be strongly bound (Section 1.4.1). Thus according to this model for CO on the $(11\bar{2}2)$ planes there will be a strongly bound β-state with a physisorbed state on top of this; there will be no α-state present.

4.3.2. $(10\bar{1}1)$ Surface

Figure 22 shows a model of CO adsorption on the $(10\bar{1}1)$ plane of ruthenium. Again the β-CO molecules are assumed to be in lying down position and CO molecules in the α-state are assumed to be in upright positions. Each CO molecule in either state is assumed to be bridge bonded to two ruthenium atoms. The ruthenium atoms donate electrons to β-CO molecules and the α-CO molecules interact with these ruthenium atoms which have already donated electrons to β-CO. Thus β-CO molecules have a negative dipole moment whereas α-CO molecules have a positive dipole moment. When all the sites for β-CO and α-CO are filled there will be no space left for any more CO molecules to come in direct contact with ruthenium atoms. Any further adsorption of CO, therefore, will be the physisorbed layer.

The $(10\bar{1}1)$ planes have two types of atomic arrangements. The arrangement given in Figure 22 seems to be the more stable one and so only this arrangement is considered in the above discussions.

4.4 Comparison with Related Works

It seems worthwhile to discuss how these results compare with those of other investigators and to compare the adsorption of carbon monoxide on ruthenium with that on tungsten. Klein (41) measured the voltage required for a constant total emission during his "flash desorption" experiments for carbon monoxide on

ruthenium and from this reported two rather "ill-defined" desorption regions, the first at 150-350°K and the second at 350-500°K. Although field desorption was used to remove carbon monoxide in the present investigation, similar curves for the voltage required for a constant emission were obtained for single crystal regions. These plots, however, do not distinctly reveal all the work function changes and corresponding adsorption states. The Fowler-Nordheim plots for single crystal regions in this research more clearly defined the adsorption states of carbon monoxide on ruthenium.

Klein (41) reported an overall increase in ϕ of ruthenium by 1.3 eV upon chemisorption of CO. The highly emitting high index regions control the slope of the F-N plot for the overall emission, and so his measured ϕ change should be similar to that measured in these studies for the high index regions. The $\Delta\phi_{ad}$ values obtained for the $(11\bar{2}2)$ and $(20\bar{2}1)$ regions after desorption of the physisorbed layers were 1.4 and 1.8 eV, respectively. These high index regions are not the highest emitting ones which may have still smaller $\Delta\phi_{ad}$ values. Thus the $\Delta\phi_{ad}$ values obtained for the high index single crystal regions are in good agreement with that reported by Klein on the overall surface.

Klein reported that CO is not as strongly chemisorbed on ruthenium as on rhenium. The following estimation of bond strength for the Ru-CO bond on ruthenium surfaces from these studies also shows that CO is bound less strongly on ruthenium than on tungsten. The observed evaporation field for ruthenium is reported to be 4.5 V/Å. Desorption (at 77°K, for 50-100 seconds) of the major chemisorption state corresponding to the large drop in emission voltage on the

$(10\bar{1}0)$ region of ruthenium occurred at desorption potentials of 99% and 92% Vc. These correspond approximately to desorption fields of 0.99 x 4.5 and 0.92 x 4.5 V/Å or 4.41 and 4.14 V/Å, respectively. Similarly, the approximate desorption fields for CO on Ru $(10\bar{1}1)$ were 4.39, 4.05 and 4.17 V/Å, and on both the Ru $(11\bar{2}2)$ and $(20\bar{2}1)$, 4.05 V/Å. According to Swanson and Gomer (15), desorption (at 60°K, for 43 seconds) of β-CO on tungsten at the coverage range corresponding to $\Delta\phi_{ad}$ values 0.18 - 0.26 eV requires a field of 4.71 V/Å. This field is higher than those required for the desorption of the major chemisorption state of CO on ruthenium indicating that CO is bound less strongly on ruthenium. However, the ratio of desorption potential of chemisorbed CO to the evaporation potential for the metal atoms is greater in the case of ruthenium than for tungsten (0.87 to 0.99 for ruthenium, 0.83 for tungsten).

Gomer, et al. (36) reported that the $\Delta\phi_{ad}$ value upon CO chemisorption on tungsten was maximum (approximately 1.25 eV) for the (211) plane. In the present investigation the $\Delta\phi_{ad}$ values after removal of the physisorbed layer were approximately 2.2, 2.3, 1.4 and 1.8 eV for the $(10\bar{1}1)$, $(10\bar{1}0)$, $(11\bar{2}2)$ and $(20\bar{2}1)$ regions, respectively. Although the $\Delta\phi_{ad}$ values are higher for ruthenium, the CO is not more strongly bound on ruthenium as pointed out in the foregoing discussions. The large change in ϕ upon adsorption of CO may be due to two reasons. First, the number of negatively charged CO molecules (β-CO) adsorbed may be greater, and second, the dipole moment of β-CO on ruthenium may be larger than that on tungsten. A larger dipole moment may not necessarily indicate stronger binding between the adsorbed molecules and the metal atoms. It is the net decrease

in energy and not the net electron transfer which contributes to the binding energy. While the metal-CO binding energy is less on ruthenium than on tungsten, nevertheless it appears to be greater in proportion to the metal-metal bonding energy on ruthenium than on tungsten. In such a case the net electron transfer from the metal orbitals to the CO orbitals will be greater on ruthenium, thereby producing a larger negative dipole moment.

For the (110) and (100) surfaces of tungsten (Figure 10), the $\Delta\phi_{ad}$ values become negative during desorption (18). The minimum $\Delta\phi_{ad}$ value for each of these two surfaces is approximately -0.15 eV. The minimum $\Delta\phi_{ad}$ values obtained for ruthenium are -2.3, -1.05, -1.85 and -0.45 eV for the $(10\bar{1}1)$, $(10\bar{1}0)$. $(11\bar{2}2)$ and $(20\bar{2}1)$ regions, respectively. Since the negative change in ϕ is attributed to the reconstruction of the substrate atoms, the reconstruction is more prominent in the case of the ruthenium surfaces. Thus while only "partial" burial of CO occurs on tungsten, "corrosive chemisorption" with burial of CO molecules even a few angstroms deep may occur on ruthenium.

The above discussions indicate many differences in adsorption of CO on ruthenium and on tungsten. However, without considering the effect of temperature, pressure and presence of hydrogen, it is not feasible to discuss the differences in catalytic activities of ruthenium and of tungsten at the present time.

4.5. Experimental Error

All the Fowler-Nordheim data were measured at a vacuum better than 1×10^{-10} torr. The measurements for each set of F-N data were finished in

approximately one minute. Therefore, any contamination from the atmosphere around the specimen may be assumed absent. The specimen was heated to about 400^{o}C for 15-30 minutes to get rid of any contamination from the shank prior to field evaporation of the tip. However, during the time of experiment and due to adsorption of CO the shank again gets contaminated. The contamination might have migrated from the shank to the specimen. This could affect the measured $\Delta\phi_{ad}$ values. Another source of inaccuracy is the impurities present in the CO gas in which the clean specimen was exposed. The impurities in ruthenium were fairly low. The only potential electron donor present was Boron (less than 10 ppm.) and no electron acceptor was reported present. Therefore, there can be no appreciable inaccuracy due to impurities in ruthenium.

Criticism of these experiments might result from the use of a spot photometer to measure the emission intensity on the fluorescent screen. For the low index regions the area measured was usually kept within the dark region on the screen. The fluorescence from other more highly emitting regions of the screen, however, most probably diffused through the phosphor to these less emitting regions, thus affecting the accuracy of the F-N data. For this reason the adsorption and desorption data are not reported for planes, but rather for regions. The measurements on the $(11\bar{2}2)$ region could be considered least affected by light diffusion through the phosphor because this region has a higher intensity in the field-emission pattern than others investigated. However, again the intensity of this region is probably considerably affected by steps on the edges of the plane.

The desorption of the same state does not occur at the same percent Vc on

all specimen (Section 3.3). The desorption and reconstruction are activated processes and thus time is an important factor. During desorption of CO the time was not controlled. The time varied from 50 to 100 seconds at each desorption potential. This may contribute to the lack of reproducibility. Secondly, the geometry of the specimen may be important. The smaller the radius of curvature, the larger will be the density of steps associated with a given area of the image. The atoms at these steps are expected to give the strongest binding in adsorption. Thus for a specimen with a small radius of curvature, a high field may be required for desorption of chemisorbed CO. Although two of the specimens used in desorption experiments on the $(10\bar{1}0)$ region had similar evaporation potentials (22.6 and 22.8 KV), the shanks of the two specimens may have been different in shape, thereby leading to similar evaporation potentials but different radii of curvature.

CHAPTER V

CONCLUSIONS AND RECOMMENDATIONS

5.1. Conclusions

The results of these adsorption and desorption experiments of carbon monoxide on the $\{10\bar{1}1\}$, $\{10\bar{1}0\}$, $\{11\bar{2}2\}$, $\{20\bar{2}1\}$ regions of ruthenium at 77°K led to the following conclusions:

1. The chemisorption of carbon monoxide on ruthenium is anisotropic; that is, the type of states present as well as the degree of interaction and/or amount of each state present varies with the crystal region.

2. The adsorption of carbon monoxide on ruthenium, in general, causes an increase in work function of each region investigated.

3. The desorption experiments of carbon monoxide on all regions investigated indicate that there is surface reconstruction causing burial of some electronegative carbon monoxide molecules and resulting in a corrosive chemisorbed layer.

4. The electronegative β-state of carbon monoxide was observed on all regions investigated while the electropositive α-state was found only on the $\{10\bar{1}1\}$ and $\{10\bar{1}0\}$ regions.

5. The changes in work function during desorption of the α-state indicate stronger interaction and/or more adsorbed α-state on the $\{10\bar{1}1\}$ region than on the $\{10\bar{1}0\}$ region.

6. Changes in work function during desorption of β-state indicate that the extent of interaction and/or the amount of adsorbed β-state decreases in the order of $\{10\bar{1}1\}$, $\{11\bar{2}2\}$, $\{10\bar{1}0\}$, and $\{20\bar{2}1\}$ regions.

7. A weakly bound electropositive physisorbed state was found on all regions investigated.

8. No decomposition of carbon monoxide absorbed on ruthenium could be detected upon adsorption or during field desorption.

5.2. Recommendations for Future Work

5.2.1. Experimental Procedure

After evacuating the chamber the specimen should be heated to a temperature such that a hemispherical tip is formed. This will cause a larger portion of the specimen to come in view. During field evaporation this will give rise to a clean surface of larger area than was obtained by field evaporating without heating the tip. This will improve the cleanliness of the tip. However, this will lead to an increase in the radius of curvature of the tip, may require high evaporation potentials, and therefore could lead to experimental difficulties.

A considerable doubt may arise from the type of emission intensity measurements done here. A probe hole technique may be used to avoid any effect on intensity of a region on the screen by some other region due to diffusion of light through the phosphor of the screen. In this technique only the electrons coming from one single crystal region is allowed to the detector by using a probe hole.

5.2.2. Further Studies

Change in surface structure, if any, upon adsorption and/or during desorption may be studied with the help of LEED. LEED studies have to be done on known ruthenium surface after cleaning, after adsorption and at various stages of desorption. The work function changes measured by FEM then can be correlated to the observed structure. FIM can also be employed to study the surface structure at cryogenic temperatures.

Temperature, pressure, and impurities may have a profound effect on and may even control the catalytic process. The next logical step in defining the role of adsorption processes in catalysis, therefore, will be to study the effect of these variables on the adsorption states.

APPENDIX

WORK FUNCTION CALCULATIONS

The Fowler-Nordheim data consist of the measured intensities of emission (I) from one region of the specimen as a function of the applied negative voltage (V). From these data, initially, I/V^2 amd $1/V$ values were calculated and the F-N plots of I/V^2 versus $1/V$ were drawn. Best fit straight line was drawn by eye estimation and the slope was measured for each F-N plot. A computer program was later developed to obtain the desired information rapidly and accurately. The data input to the computer consisted of the number of points in the F-N plot, the field evaporation voltage, the field desorption voltage and the V and I values. The computer output consisted of the slope, the ln A values, standard deviation, $(\text{slope})^{2/3}$, desorption potential as percent Vc and "normalized" $(\text{slope})^{2/3}$ value. (Least square method was used for this analysis. The computer program (ALGOL) is given below.) In the output, the $(\text{slope})^{2/3}$ value is given in the column under "WK FCN;" ln A is under "INTCPT" column. The slopes of two different regions of the same specimen evaporated at potentials of almost equal magnitude will be related to each other by:

$$\phi_1/\phi_2 = (\text{slope}_1)^{2/3}/(\text{slope}_2)^{2/3}. \qquad (15)$$

Thus if the ϕ value of one region (ϕ_1) is known and the $(\text{slope}_1)^{2/3}$ and $(\text{slope}_2)^{2/3}$

values obtained from the computer, the work function of the unknown region (ϕ_2) can be calculated.

Similarly, if the $(\text{slope})^{2/3}$ values for a clean region and for the region with adsorbed carbon monoxide are measured and if the ϕ value of the clean region is known, then the work function of the carbon monoxide covered surface can be calculated.

The Computer Program (ALGØL)

```
BEGIN
FILE SBIN----;
FILE SBØUT----;
INTEGER I, N;
REAL INTCPT, SLØPE, STANDARDDEVIATIØN, S5, WF, WFN, FEV, FD, PD;
ARRAY V, R, X, Y, YCALC, DIFF1[O:20];

FØRMAT FT1(/, X7, "SLØPE", X5, "INTERCEPT", X5, "ST DEV", X6, "WK FCN, X2,
"N W F", X2, "F E V", X2, "PC V D");
FØRMAT FT2(X2, E12.5, X2, E12.5, X2, E12.5, X1, F6.3, X1, F5.2,
X2, F5.2, X2, F6.2);
FØRMAT FT4(X5, "INTERCEPT IS NEGATIVE"/);
LABEL ØVER, ALL;
PRØCEDURE LSTSQR(X, Y);
ARRAY X, Y[*];
BEGIN
REAL SUMX, SUMY, SUMXY, SUMX2;
SUMX:=SUMY:=SUMXY:=SUMX2:=S5:=0;
FØR I:=1 STEP 1 UNTIL N DØ
BEGIN
SUMX:=SUMX + X[I];
SUMX:=SUMY + Y[I];
SUMXY:=SUMXY + X[I]×Y[I];
SUMX2:=SUMX2 + X [I]*2 END;
INTCPT:=(SUMXY×SUMX - SUMX2×SUMY)/(SUMX*2 - N×SUMX2);
SLØPE:=(SUMX×SUMY - N×SUMXY)/(SUMX*2 - N×SUMX2);
IF SLØPE ≥ 0 THEN WF:=SLØPE*(2/3);
IF FEV ≥ FD THEN WFN:=((SLØPE×10)/FEV)*(2/3)
ELSE WFN:=((SLØPE×10)/FD)*(2/3);
```

```
PD:=100*FD/FEV;
FOR I:=1 STEP 1 UNTIL N DO
BEGIN
YCALC[I]:=INTCPT*SLOPE*X[I];
DIFF1[I]:=YCALC[I]-Y[I];
S5:=S5+DIFF1[I]*2;
END;
STANDARDDEVIATION←SQRT(S5/(N-2));
IF INTCPT≤0 THEN WRITE(SBOUT, FT4)
END;
WRITE(SBOUT, FT1);
OVER:  READ(SBIN, /, FEV, FD, N, FOR I:=1 STEP 1 UNTIL N
  DO [V[I], R[I] ])[ALL];
FOR I:=1 STEP 1 UNTIL N DO  BEGIN
X[I]:=-1/V[I];
Y[I]:=LN(R[I]/V[I]*2);
END;
LSTSQR(X, Y);
WRITE(SBOUT, FT2, SLOPE,  INTCPT, STANDARDDEVIATION, WF, WFN, FD, PD);
GO TO OVER;
ALL:END.
```

BIBLIOGRAPHY

1. H. E. Grenga, "Active Sites for the Catalytic Decomposition of Carbon Monoxide on Nickel," Ph.D. Dissertation, University of Virginia (1967).

2. J. T. Ratliff, "Early Stages in the Interaction of Carbon Monoxide with Iron Single Crystal Films," Ph.D. Dissertation, Georgia Institute of Technology (1968).

3. H. Leidheiser and A. T. Gwathmey, J. Amer. Chem. Soc., 70 (1948), 1206.

4. R. E. Cunningham and A. T. Gwathmey, Adv. in Catalysis, 9 (1957), 25.

5. E. Cox, K. R. Lawless and A. T. Gwathmey, Actes du Deuxieme Congress International de Catalyse, Editions Technip, Paris, 1961.

6. R. Gomer, "Field Emission and Field Ionization," Harvard University Press, Cambridge, Massachussetts, 1961.

7. R. H. Fowler and L. W. Nordheim, Proc. Roy. Soc. (London), A911 (1928), 173.

8. D. Menzel and R. Gomer, J. Chem. Phys., 41 (1964), 3311.

9. A. G. J. Van Oostrom, Thesis, Amsterdam (1965).

10. A. A. Holscher, "Adsorption Studies with the Field-Emission and Field-Ion Microscope," Thesis, Amsterdam (1967).

11. B. Ralph and M. J. Southton, Science Journal, Feb. 1966, 50.

12. E. W. Müller, Phys. Rev., 102 (1956), 618.

13. E. W. Müller, Adv. in Electronics and Electron Physics, Edited by L. Marton, Academic Press, 13 (1960), 83.

14. E. W. Müller, Natwiss., 29 (1941), 533.

15. L. W. Swanson and R. Gomer, J. Chem. Phys., 39 (1963), 2813.

16. C. A. Coulson, Valence, (2nd Ed.), Oxford Univ. Press, London and New York (1961).

17. G. Blyholder, J. Phy. Chem., 68 (1964), 2772.

18. R. R. Ford, Advan. Catal. Relat. Subj. 21 (1970), 51.

19. F. C. Tompkins, The Solid-Gas Interface, Edited by E. Alison Flood, Marcel Dekker, Inc., New York, 1967.

20. C. Kohrt and R. Gomer, Surface Sc., 24 (1971), 77.

21. C. R. Guerra and J. H. Schulman, Surface Sc., 7, (1967), 229.

22. N. N. Kavtardze and N. P. Sokolova, Dokl. Acad. Nauk SSSR, 162 (1965), 847.

23. N. N. Kavtardze and N. P. Sokolova, Zhur. Fiz. Khim., 40 (1966), 2957.

24. N. N. Kavtardze and N. P. Sokolova, Zhur. Fiz. Khim., 41, (1967)

25. D. O. Hayward and B.M.W. Trapnell, Chemisorption, Butterworths, Washington (1964).

26. G. Blyholder, J. Phy. Chem., 68 (1964), 2772.

27. L. Lynds, Spectrochimia Acta, 20, (1964), 1369.

28. P. A. Redhead, Trans. Faraday Soc., 57 (1961), 641.

29. R. P. Eischens, The Surface Chemistry of Metals and Semiconductors, Edited by H. C. Gates, John Wiley and Sons, New York, (1960), 421.

30. M. A. Lanyon and B.M.W. Trapnell, Proc. Roy. Soc., A227 (1955), 387.

31. D. J. C. Yates and C. W. Garland, J. Phy. Chem, 65 (1961), 617.

32. A. M. Bradshaw and O. Vierle, Ber. Bunsenges. Phys. Chem., 74 (1970), 630.

33. L. C. Ferreira and E. C Leisengang, J. S. Afr. Chem. Int., 23 (1970), 136.

34. J. Anderson and P. J. Estrup, J. Chem. Phys., 46 (1967), 563.

35. D. O. Hayward and B.M.W. Trapnell, Chemisorption, Butterworths (1964).

36. T. Engel and R. Gomer, J. Chem. Phys., 50 (1969), 2428.

37. R. P. H. Gasser, R. Thwaites and J. Wilkinson, Trans. Faraday Soc., 63 (1967), 195.

38. M. P. Hill, Trans. Faraday Soc. (1969), 1246.

39. J. W. May and L. H. Germer, J. Chem. Phys., 44 (1966), 1065.

40. R. Klein and L. B. Leder, J. Chem. Phys., 38 (1963), 1866.

41. R. Klein, Surface Sc., 20 (1970), 1.

42. R. Gomer and A. A. Bell, J. Chem. Phys., 44 (1966), 1065.

43. L. H. Germer and A. W. MacRae, Proc. Natl. Acad. Sci., 48 (1962), 997.

44. L. H. Germer, E. J. Scheibner and C. D. Hartman, Phil. Mag., 5 (1960), 222.

45. R. L. Park and H. E. Farnsworth, J. Chem. Phys., 40 (1964), 2354.

46. H. E. Farnsworth and H. H. Madden, J. Appl. Phys., 32 (1961), 1933.

47. H. E. Farnsworth and D. M. Zeihner, Surface Sc., 17 (1969), 7.

48a. R. O. Adams } The Structure and Chemistry of Solids, Edited by G. A.
48b. T. W. Hass } Somerjai, Wiley, New York (1969).

49. T. W. Hass, A. G. Jackson and M. P. Hooker, J. Chem. Phys., 46 (1967), 3025.

50. G. A. Somerjai and F. J. Szalkowski, J. Chem. Phys., 54 (1971), 389.

51. J. C. Tracy and P. W. Palmberg, J. Chem. Phys., 51 (1969), 4852.

52. G. Art and J. Koch, Z. Naturforsch., 25a (1970), 1906.

53. E. M. Savitskii, L. H. Litvak, I. V. Burov, V. P. Polyakova and G. D. Shnyrev, Dokl. Akad. Nauk. SSSR, 197 (1970), 783.

54. R. W. Newman, R. C. Sanwald, and J. J. Hren, J. Sci. Instrum., 44 (1967), 828.

55. T. E. Madey and J. T. Yates, Jr., Nuovo Cimento Suppl., 5 (1967), 483.